

This discussion paper is/has been under review for the journal Atmospheric Chemistry and Physics (ACP). Please refer to the corresponding final paper in ACP if available.

Properties of young contrails – a parametrisation based on large eddy simulations

S. Unterstrasser

Deutsches Zentrum für Luft- und Raumfahrt (DLR), Institut für Physik der Atmosphäre,
Oberpfaffenhofen, 82234 Wessling, Germany

Received: 7 August 2015 – Accepted: 11 October 2015 – Published: 27 October 2015

Correspondence to: S. Unterstrasser (simon.unterstrasser@dlr.de)

Published by Copernicus Publications on behalf of the European Geosciences Union.

ACPD

15, 28939–28997, 2015

Properties of young
contrails –
a parametrisation
based on large eddy
simulations

S. Unterstrasser

[Title Page](#)

[Abstract](#)

[Introduction](#)

[Conclusions](#)

[References](#)

[Tables](#)

[Figures](#)

◀

▶

[Back](#)

[Close](#)

[Full Screen / Esc](#)

[Printer-friendly Version](#)

[Interactive Discussion](#)

Abstract

Contrail-cirrus is probably the largest climate forcing of aviation. The evolution of contrail-cirrus and their radiative impact depends on a multitude of atmospheric parameters, but also on the geometric and microphysical properties of the young contrails evolving into contrail-cirrus. The early evolution of contrails ($t < 5$ min) is dominated by an interplay of ice microphysics and wake vortex dynamics. Young contrails may undergo a fast vertical expansion due to a descent of the wake vortices and may lose a substantial fraction of their ice crystals due to adiabatic heating. The geometric depth H and total ice crystal number N of young contrails are highly variable and depend on many environmental and aircraft parameters. Both properties, H and N , affect the later properties of the evolving contrail-cirrus, as they control the extent of shear-induced spreading and sedimentation losses. In this study, we provide parametrisations of H and N after 5 min taking into account the effects of temperature, relative humidity, thermal stratification and aircraft type (mass, wing span, fuel burn). The parametrisations rely on a large data set of recent large-eddy simulations of young contrails. They are suited to be incorporated in larger-scale models in order to refine the present day contrail initialisations by considering the processes that strongly affect the contrail evolution during the vortex phase.

1 Introduction

20 1.1 Motivation

Contrail-cirrus is probably the largest contribution of aviation to climate change in terms of radiative forcing (Burkhardt and Kärcher, 2011). However, its quantification is associated with large uncertainties and the confidence of those estimates is still rated low (Boucher et al., 2013). Contrail radiative forcing is estimated by global circulation models (GCMs) whose parametrisations of contrails have been improved in the re-

[Title Page](#)[Abstract](#)[Introduction](#)[Conclusions](#)[References](#)[Tables](#)[Figures](#)[|◀](#)[▶|](#)[◀](#)[▶](#)[Back](#)[Close](#)[Full Screen / Esc](#)[Printer-friendly Version](#)[Interactive Discussion](#)

cent past. In particular, the analysis methods switched from diagnostic approaches for young (line-shaped) contrails (Ponater et al., 2002; Rap et al., 2010; Chen and Gettelman, 2013) towards a process based treatment of contrail cirrus evolution (Burkhardt and Kärcher, 2009; Schumann, 2012).

- 5 Contrail microphysical, geometric and optical properties depend on a multitude of meteorological and aircraft parameters as investigated by high resolution simulations (Lewellen, 2014; Unterstrasser and Görsch, 2014). In the first few minutes of contrail lifetime, the contrail evolution is strongly affected by the downward propagating wake vortex pair. On the one hand, this can lead to a substantial increase in contrail depth.
- 10 On the other hand, adiabatic heating may result in strong crystal loss. Both processes have an impact on the evolution of the contrail-cirrus while it spreads by vertical wind shear and produces a fall streak by sedimentation.

15 The present study develops and provides a parametrisation for the depth and crystal number of young contrails which accounts for the important physics and considers the dominant parameters, namely relative humidity, temperature, thermal stratification and aircraft parameters. The parametrisation is based on the evaluation of a large data set of recent large-eddy simulations (LES). Due to its simple analytic form it is suited to be incorporated in large-scale models where it can replace present day contrail initialisation with ad-hoc assumptions where vortex phase processes are only very

20 roughly captured. This approach exhibits a way to condense information gained from LES such that it finds its way into global scale models.

The presented parametrisation covers a much larger parameter space and is more universal than the parametrisation given by Unterstrasser et al. (2008) and extended by Kärcher et al. (2009). Clearly, the present work updates the earlier versions.

25 In the recent past, the effect of biofuels on contrail properties aroused scientific interest. In particular, the likely reduction in the initial ice crystal number can have a significant effect, even though the initial differences in ice crystal number are reduced during the vortex phase (Lewellen, 2014; Unterstrasser, 2014). The effect of biofuels may be

Properties of young contrails – a parametrisation based on large eddy simulations

S. Unterstrasser

[Title Page](#)

[Abstract](#)

[Introduction](#)

[Conclusions](#)

[References](#)

[Tables](#)

[Figures](#)

[|◀](#)

[▶|](#)

[◀](#)

[▶](#)

[Back](#)

[Close](#)

[Full Screen / Esc](#)

[Printer-friendly Version](#)

[Interactive Discussion](#)



Title Page

Abstract

Introduction

Conclusions

References

Tables

Figures

◀

▶

◀

▶

Back

Close

Full Screen / Esc

Printer-friendly Version

Interactive Discussion

overestimated, if crystal loss is neglected. The presented parametrisation accounts for the crystal loss, hence it avoids this problem.

Moreover, the present approach complements a parametrisation describing the long term contrail-cirrus evolution in Lewellen (2014) where the ice crystal number is an important input parameter.
5

1.2 Contrail microphysics and dynamics

Since the design of the proposed parametrisations is motivated by the physical processes involved in contrail evolution, this section will give a short overview over various aspects of the contrail evolution. In the remainder of the text, we assume that the environment is sufficiently cold and moist, such that contrails form (Schumann, 1996) and persist (i.e. that the air is supersaturated). In general, contrail development is divided into three temporal phases based upon the governing physical processes, the jet, vortex and dispersion phase (Hoshizaki et al., 1975).

The jet phase denotes the first several seconds, in which the lift generating airflow over the wings transforms into a counter-rotating vortex pair. The hot exhaust jets mix with the cold ambient air, expand and get entrained into the forming vortices (Paoli et al., 2013). Formation of ice crystals is completed within one second behind the aircraft and their number N_{form} depends inter alia on the number of emitted soot particles N_{soot} (Kärcher and Yu, 2009). Both quantities are usually given in units “number per metre (of flight path)”.

In the vortex phase, which lasts several minutes, the counter-rotating vortices propagate downward up to several hundreds of metres. Whereas most of the exhaust (including the ice crystals) is carried down in the vortex system (called primary wake), some of it gets detrained and forms a curtain between the cruise altitude and the actual vortex position (called secondary wake). After vortex break-up, buoyancy may cause that a major fraction of the exhaust rises back to original emission altitude (e.g. Unterstrasser et al., 2014). Ice crystals sublime and get lost due to adiabatic heating in the primary wake (Sussmann and Gierens, 1999). The number of ice crystals surviving
25

the vortex phase, N , is highly variable and depends on a multitude of environmental conditions and aircraft properties (Lewellen et al., 2014; Lewellen, 2014; Unterstrasser, 2014; Unterstrasser and Görsch, 2014). Ice crystals in the secondary wake face the fresh supersaturated air and grow, such that they often contain most of the contrail ice mass at the end of the vortex phase.

The dispersion phase treats the contrail-to-cirrus transition and starts once the vortices have lost their coherent structure and vorticity has reached ambient levels. Besides the environmental conditions during this transition, the early contrail properties matter for the later contrail-cirrus properties (Unterstrasser and Gierens, 2010a, b; 10 Lewellen, 2014; Unterstrasser, 2014; Unterstrasser and Görsch, 2014). More specifically, Unterstrasser and Görsch (2014) investigated the impact of aircraft type on contrail-cirrus evolution. There, contrails differed a lot in terms of vertical extent and ice crystal number after the vortex phase and simulation tests showed that both the contrail depth and ice crystal number after the vortex phase are relevant for the later 15 properties of the contrail-cirrus.

Compared to time scale of natural processes like vertical turbulent mixing, the initial expansion during the vortex phase can be viewed as a sudden event. The extent of the shear-induced horizontal spreading scales linearly with the contrail depth. Later, the depth of contrail-cirrus will increase by sedimentation and the formation of a fall 20 streak given that the supersaturated layer is sufficiently deep. Moreover, radiative lifting may increase the contrail vertical extent (Lewellen, 2014; Unterstrasser and Gierens, 2010b). The effectiveness of sedimentation depends on the ice crystal size distribution. In a simplified picture (where we think of a monodispersed size distribution of the ice 25 crystals), the size is determined by contrail ice mass and ice crystal number. As the ice mass of the emerging contrail-cirrus is mainly controlled by the supply of ambient water vapour, contrail cirrus properties are more susceptible to changes of number than mass of the young contrail (Unterstrasser and Gierens, 2010b). Thus, our study focuses on ice crystal number N rather than ice crystal mass $/$.

Properties of young contrails – a parametrisation based on large eddy simulations

S. Unterstrasser

[Title Page](#)

[Abstract](#)

[Introduction](#)

[Conclusions](#)

[References](#)

[Tables](#)

[Figures](#)

[|◀](#)

[▶|](#)

[Back](#)

[Close](#)

[Full Screen / Esc](#)

[Printer-friendly Version](#)

[Interactive Discussion](#)

The number of ice crystals after the vortex phase N is given by

$$N_{\text{surv}} = N_{\text{form}} \times f_{Ns}, \quad (1)$$

where f_{Ns} is the fraction of ice surviving the vortex phase (“survival fraction”). N_{form} is the number of generated ice crystals in the beginning and is given by

$$N_{\text{form}} = \frac{\dot{m}_f}{U} EI_{iceno}, \quad (2)$$

where EI_{iceno} is the “emission” index of ice crystals. In soot-rich regimes, homogeneous freezing of water-activated soot is the primary ice formation mechanism (Kärcher and Yu, 2009) and EI_{iceno} may be given by $f_A \times EI_{soot}$, where f_A is the fraction of activated soot particles. A schematic overview is given in Fig. 1. Evaluation of f_A and the corresponding soot emission index EI_{soot} is left to others (Kärcher et al., 1998; Kärcher and Yu, 2009). In this paper, we simply vary EI_{iceno} and parametrise f_{Ns} .

Section 2 describes the data set of simulations and explains the vortex phase processes in more detail. Section 3 presents analytical parametrisations of the survival fraction, the depth and the width of 5 min old contrails. Section 4 discusses the relevance of the input parameters and the effects of a soot reduction. Section 5 discusses the robustness of the presented parametrisations and conclusions are drawn in Sect. 6.

Throughout the paper, parametrisations and fit functions are identified by an $\hat{\cdot}$ -symbol like \hat{f}_{Ns} or \hat{N}_{surv} .

2 Data set of large-eddy simulations

The parametrisation is based on 3-D LES simulations of the contrail vortex phase with EULAG-LCM (Söhlch and Kärcher, 2010) that are described in two recent publications (Unterstrasser, 2014; Unterstrasser and Görsch, 2014). Additionally, several EI_{iceno} -sensitivity simulations not yet published are considered.

[Title Page](#)
[Abstract](#)
[Introduction](#)
[Conclusions](#)
[References](#)
[Tables](#)
[Figures](#)
[|◀](#)
[▶|](#)
[Back](#)
[Close](#)
[Full Screen / Esc](#)
[Printer-friendly Version](#)
[Interactive Discussion](#)

Title Page	
Abstract	Introduction
Conclusions	References
Tables	Figures
◀	▶
◀	▶
Back	Close
Full Screen / Esc	
Printer-friendly Version	
Interactive Discussion	

The simulations start at wake age of several seconds. Then it is reasonable to assume ice crystal nucleation and wake vortex roll-up to be finished. A pair of counter-rotating Lamb Oseen vortices with specified circulation Γ_0 is prescribed together with two circular plumes containing N_{form} ice crystals. A more detailed description of the simulation set-up is given in the aforementioned references.

A list of all 81 simulations is given in Table A2. Columns 2–7 summarise those parameters of the simulations that are incorporated in the parametrisation:

- temperature at cruise altitude T_{CA}
- ambient relative humidity RH_i or supersaturation $s_i = \text{RH}_i - 1$
- Brunt–Väisälä frequency N_{BV}
- aircraft (AC) type
- water vapour emission
- ice crystal “emission” index EI_{iceno}

Variations of T_{CA} , RH_i , EI_{iceno} and fuel flow have a direct impact on contrail ice microphysics and do not affect the wake vortex evolution as latent heating effects are negligible. Those variations have been examined in Unterstrasser (2014) (from now on referred to as U2014) for a contrail generated by an aircraft of type B777/A340. Variations of N_{BV} and AC type mainly affect the wake vortex evolution and have been examined in Unterstrasser and Görsch (2014) (from now on referred to as UG2014).

We will shortly describe a few parameter studies selected from these two publications. This should illustrate the basic microphysical and dynamical mechanisms, exemplify the impact of the above mentioned parameters and point out the processes leading to the variability in H and N_{surv} .

Figure 2 shows vertical profiles of ice crystal number after 5 to 6 min, i.e. at a time the vortices have already broken up and the contrail reached its full vertical extent (for

now neglecting the later formation of a fall streak). Such plots have been used to determine the final vertical displacement Z_{desc} of the wake vortex and the contrail depth H . Having in mind likely future applications of the parametrisations in large scale models, where physics of the contrail-cirrus transition are anyway more simplified than in LES approaches, uncertainties of $\pm 25 \text{ m}$ in the H -determination are certainly acceptable.

The left panel shows the effect of a RH_i -variation. The evolution of the wake vortex pair is unaffected by such a variation. Hence, the final vertical displacement Z_{desc} (marked by the black bar) is basically identical. In this specific case, ice crystal loss either reduces the contrail depth H ($\text{RH}_i \leq 110\%$) or the crystal abundance in the primary wake ($\text{RH}_i = 120\%$). Thus, contrail depth H depends on RH_i and the boxes show our choices of H values.

Due to adiabatic heating in the primary wake, sublimation and loss of ice crystals occurs even in a supersaturated environment. Figure 3a shows the normalised ice crystal number $f_N(t) = N(t)/N_{\text{form}}$ over time. Once the vortex descent stops after a few minutes, the rapid crystal loss ceases and the f_N -value at the end of the simulation defines the survival fraction f_{Ns} . For the given RH_i -variation, f_{Ns} ranges from less than 5 % to more than 90 %.

As a next step, contrails of six different aircraft types were investigated in UG2014. This ranged from a regional airliner Bombardier CRJ to the largest passenger aircraft Airbus A380. The wing span, mass, speed and fuel flow of the aircraft determines the circulation and the separation of the wake vortices, the water vapour emission and the number of ice crystals (for a given EI_{iceno}). The specific aircraft-dependent choices in UG2014 rely on BADA estimates (Nuic, 2011). Table 1 lists the most relevant aircraft-dependent properties. More details are listed in Table 1 of UG2014.

The right panel of Fig. 2 illustrates the impact of AC type and thermal stratification on the wake vortex evolution. For the displayed $\text{RH}_i = 140\%$ -simulations, crystal loss is low (not shown) and the contrail profiles reveal the final vertical displacement Z_{desc} of the vortices. Z_{desc} is larger for larger aircraft and weaker stratification. The trends in contrail depth are the same. Note that for stronger stratification, buoyancy effects are

Properties of young contrails – a parametrisation based on large eddy simulations

S. Unterstrasser

[Title Page](#)

[Abstract](#)

[Introduction](#)

[Conclusions](#)

[References](#)

[Tables](#)

[Figures](#)

[|◀](#)

[▶|](#)

[Back](#)

[Close](#)

[Full Screen / Esc](#)

[Printer-friendly Version](#)

[Interactive Discussion](#)

stronger and more ice crystals are pushed back to cruise altitude (CA). For the A380 aircraft, these restoring forces even lead to an overshooting and the contrail may reach altitudes nearly 100 m above the CA.

The different wake vortex evolutions have consequences on the crystal loss extent and more crystals are lost for larger Z_{desc} as adiabatic heating is stronger. Thus, fewer ice crystals are lost in a more stable environment and for smaller aircraft as Fig. 3b demonstrates for $RH_i = 120\%$ -cases. Nevertheless, a A380-contrail contains more ice crystals than a CRJ-contrail, as the fuel flow is higher and thus N_{form} is larger assuming an aircraft-independent value for EI_{iceno} .

Finally, the effect of an EI_{iceno} -variation is discussed. Figure 4 shows the temporal evolution of ice crystal mass (top) and number (middle) for various EI_{iceno} -values. The higher EI_{iceno} and N_{form} are, the smaller is the mean mass of the ice crystals. Thus, a larger fraction of them is lost. There is a subtle difference in the way EI_{iceno} affects f_N compared to RH_i or T_{CA} and will later be reflected in the design of the parametrisation. Variation of the latter two variables affects the ice mass evolution (see Fig. 3 in U2014, e.g.) which then has implications on the number evolution. For a EI_{iceno} -variation, on the other hand, the ice mass evolution is basically identical. Note that the differences after two minutes are mostly due to different growth of detrained crystals in the secondary wake, which is irrelevant for the number loss in the primary wake. This has also implications on the contrail depth. Figure 4 bottom shows vertical profiles of ice crystal mass. The contrail depth is unaffected by a variation of EI_{iceno} and by the implied change in crystal loss.

In Sect. 3.3 of U2014, the width r_{SD} of the initial ice crystal size distribution was varied and the effect of an r_{SD} -variation is similar to that of an EI_{iceno} -variation, i.e. the mass budget and the contrail depth are unaffected, but the extent of crystal loss changes. This suggests that contrail depth is only affected by parameter variations that change the mass evolution or the wake vortex evolution.

Title Page

Abstract

Introduction

Conclusions

References

Tables

Figures

|◀

▶|

Back

Close

Full Screen / Esc

Printer-friendly Version

Interactive Discussion

3 Parametrisation

Title Page	
Abstract	Introduction
Conclusions	References
Tables	Figures
◀	▶
◀	▶
Back	Close
Full Screen / Esc	
Printer-friendly Version	
Interactive Discussion	

The examples in the preceding section highlighted some basic mechanisms. This section provides the theoretical background to better understand the observed sensitivities and allow the development of process-based parametrisations for the survival fraction and the contrail depth. For the contrail-to-cirrus transition the ice crystal number matters, which is the product of initial ice crystal number and survival fraction.

3.1 Characteristic length scales

We introduce three length scales that help to understand and explain the observed processes in a young contrail. A similar attempt has already been undertaken in Unterstrasser et al. (2008), where three time scales were used to better explain the observed processes in the downward sinking contrail. The three length scales are:

- z_{desc} which measures the final vertical displacement of the wake vortex,
- z_{atm} which measures the effect of the ambient supersaturation on the ice crystal mass budget,
- z_{emit} which measures the effect of the water vapour (WV) emission on the ice crystal mass budget.

We will later see that the approximations of f_{Ns} and H take simple forms, if expressed in terms of z_{Δ} , which is a linear combination of the three length scales:

$$z_{\Delta} = \alpha_{\text{atm}} \times z_{\text{atm}} + \alpha_{\text{emit}} \times z_{\text{emit}} - \alpha_{\text{desc}} \times \hat{z}_{\text{desc}} \quad (3)$$

- with positive weights α_i . The equation describes a balance between the WV surplus (raising RH_i) and wake vortex induced adiabatic heating (lowering RH_i). Note the minus sign in front of the \hat{z}_{desc} -term. In the following, we will define the three length scales. Whereas z_{atm} and z_{emit} are analytically defined, z_{desc} is determined from simulations and an analytical approximation \hat{z}_{desc} enters the balance Eq. (3).

3.1.1 Length scale z_{desc}

In scenarios with $\text{RH}_i = 140\%$ contrails reach their full vertical extent, as ice crystal loss is small. The determination of z_{desc} is based on visually inspecting vertical profiles of such simulations (as exemplified in Fig. 2). Following UG2014 or a shortened derivation in Sect. A2, z_{desc} can be approximated by

$$\hat{z}_{\text{desc}} = \sqrt{\frac{8\Gamma_0}{\pi N_{\text{BV}}}} \quad (4)$$

\hat{z}_{desc} depends solely on Γ_0 and N_{BV} . Γ_0 denotes the initial circulation of the wake vortices. It can be computed via Eq. (A1) or empirically determined via Eq. (A5). Compared to a variation of the aircraft type (affecting Γ_0) and the ambient stratification, variations of vertical wind shear and turbulence are of secondary importance (at least for stratification values typical of the upper troposphere), see e.g. Unterstrasser et al. (2014).

3.1.2 Length scale z_{atm}

We consider a supersaturated air parcel that we assume to be void of ice-crystals, i.e. no deposition/sublimation is going on. Then we estimate the vertical displacement z_{atm} of the parcel that is necessary to reduce the relative humidity to saturation. This means that the water vapour concentration of a supersaturated air parcel is equal to that of a saturated parcel at some higher temperature. Using the ideal gas law $\rho_v = \frac{e_v(T)}{R_v T}$, we then have:

$$(1 + s_i) \frac{e_s(T_{\text{CA}})}{T_{\text{CA}}} = \frac{e_s(T_{\text{CA}} + \Gamma_d z_{\text{atm}})}{(T_{\text{CA}} + \Gamma_d z_{\text{atm}})} \quad (5)$$

with supersaturation s_i , saturation vapour pressure e_s and dry adiabatic lapse rate Γ_d . The non-linear equation in z_{atm} is solved using a simple iterative numerical approach.

[Title Page](#)

[Abstract](#)

[Introduction](#)

[Conclusions](#)

[References](#)

[Tables](#)

[Figures](#)

[|◀](#)

[▶|](#)

[◀](#)

[▶](#)

[Back](#)

[Close](#)

[Full Screen / Esc](#)

[Printer-friendly Version](#)

[Interactive Discussion](#)

A similar, yet linearised version of this definition was given in Unterstrasser et al. (2008) (there named δ_{crit}).

Table A2 lists the values of z_{atm} for given RH_i and T_{CA} and shows the dominant impact of RH_i .

- 5 Using the wake vortex descent speed w , z_{atm} can be converted into a time scale t_{atm} which gives the link to the observed RH_i -separated onset of crystal loss in Fig. 3a.

3.1.3 Length scale z_{emit}

We consider an ice crystal-free saturated aircraft plume. Then the emitted water vapour increases the vapour concentration ρ in the plume such that it is supersaturated. The 10 water vapour emission \mathcal{V} (in units kg m^{-1} (of flight path)) is determined mainly by the fuel flow of the aircraft, see Eq. (A8). The additional water vapour can be seen as an additional concentration

$$\rho_{\text{emit}} = \frac{\mathcal{V}}{A_p} \quad (6)$$

assuming a uniform distribution over a certain plume area A_p . An aircraft-dependent 15 approximation of the plume area is given in Sect. A4. Similar to the z_{atm} -derivation, we determine the vertical displacement z_{emit} that is necessary to reduce the relative humidity to saturation.

$$\frac{e_s(T_{\text{CA}})}{R_v T_{\text{CA}}} + \rho_{\text{emit}} = \frac{e_s(T_{\text{CA}} + \Gamma_d z_{\text{emit}})}{R_v (T_{\text{CA}} + \Gamma_d z_{\text{emit}})} \quad (7)$$

The non-linear equation in z_{emit} is solved using a simple iterative numerical approach.

20 Both quantities, A_p and \mathcal{V} scale with b^2 , such that ρ_{emit} and z_{emit} are nearly independent of the AC type. Table A2 lists the values of z_{emit} which shows a strong impact of T_{CA} and the second order effect of AC type.

Figure 3c shows the ice crystal number evolution for various temperatures. Whereas the onset of crystal loss is similar (unlike to cases, when RH_i is varied), crystal loss is

Title Page

Abstract

Introduction

Conclusions

References

Tables

Figures

◀

▶

◀

▶

Back

Close

Full Screen / Esc

Printer-friendly Version

Interactive Discussion

faster for higher temperature. This is simply due to the fact the derivative $\frac{d}{dT}e_s$ is higher at higher temperature and more ice mass has to sublime to maintain saturation.

We see in our simulations that the ice and water vapour are not homogeneously distributed over the plume. Thus, our picture of a uniform bulk- ρ_{emit} may be overly simple, if the effects of plume inhomogeneity on crystal loss do not average out.

Moreover, the plume area is only vaguely determined in our approach. We neglect, e.g., the possible impact of stratification which affects the detrainment of ice crystals out of the vortices and the entrainment of ambient air into the vortices.

One the other hand, a possible systematic underestimation of A_p , e.g., would result in an overestimation of q_{emit} and z_{emit} . Our parametrisation is designed in way that such a bias can be compensated by choosing a smaller value for weight α_{emit} .

We will later demonstrate that the present approach is advanced enough to capture the most relevant dependencies.

3.2 Crystal loss

The latter two length scales were introduced assuming an ice crystal free parcel, yet they are also meaningful for an ice crystal laden plume. Then, the excess moisture (WV emission + ambient supersaturation) quickly deposits on the ice crystals such that relative humidity reaches saturation and the ice mass is the sum of both contributions. Ongoing heating of the plume causes a slight subsaturation and sublimation of ice mass. After a downward displacement of z_{atm} , the ice crystals have lost as much mass as was contributed by the ambience (neglecting a small time delay); that is, the remaining ice mase equals that of the WV emission.

The left panel of Fig. 5 depicts the simulated f_{Ns} -values as a function of z_Δ for several subsets of simulations. The choice of the weights α_i for the computation of z_Δ will be discussed later. We approximate f_{Ns} by an arc tangent function (grey curve) which

Title Page	
Abstract	Introduction
Conclusions	References
Tables	Figures
◀	▶
◀	▶
Back	Close
Full Screen / Esc	
Printer-friendly Version	
Interactive Discussion	

depends solely on z_Δ . The approximated survival fraction \hat{f}_{Ns} is defined by

$$\hat{f}_{Ns} = \hat{a}(z_\Delta) \text{ where} \quad (8)$$

$$\hat{a}(x) = \beta_0 + \frac{\beta_1}{\pi} \arctan(\alpha_0 + (x/100\text{m})). \quad (9)$$

Values of \hat{a} below 0 and above 1 are clipped. Again, values of the fit parameters β_0, β_1 and α_0 are provided later.

The first row of Fig. 5 shows f_{Ns} for a basic $RH_i - T_{CA}$ -variation for one AC type. The selected simulations are listed in block 1 of Table A2 and all have the same \hat{z}_{desc} . Z_{atm} and z_{emit} vary over large ranges, as they mainly depend on RH_i and T_{CA} . Thus, this sub panel demonstrates that the RH_i - and T_{CA} -sensitivity of f_{Ns} is well captured by our $\hat{a}(z_\Delta)$ -approach.

In a next step, the AC type is varied (block 2/row 2 of the table/figure). The aircraft type strongly affects the wake vortex properties, i.e. the descent speed, the time of vortex break-up and the final vertical displacement. Thus, this simulation subset focuses on the variation of z_{desc} (and Z_{atm}). f_{Ns} is smaller for larger aircraft. This trend is also captured by the approximation, as \hat{z}_{desc} is larger and, correspondingly, z_Δ is smaller.

Row 3 of the figure extends the simulation set by cases with weaker stratification where z_{desc} is larger and fewer ice crystals survive. The approximation is able to predict the behaviour, yet the distances between the data points and the approximation are larger than in row 1.

So far, the prediction of ice crystal number loss is based on a balance equation of the ice crystal mass. This is suitable and works for the simulations depicted in rows 1–3, as they all use the reference ice crystal emission index $EI_{iceno, ref} = 2.8 \times 10^{14} \text{ kg}^{-1}$. In these cases a certain ice mass change can be linked to a certain ice crystal loss. As discussed in Sect. 2, this does not hold any longer, when EI_{iceno} is varied. To cover the effects of a EI_{iceno} -variation, the parametrisation must be extended. Note that, so far EI_{iceno} did not enter the computations for the length scales, z_Δ nor for \hat{a} .

Title Page

Abstract

Introduction

Conclusions

References

Tables

Figures

|◀

▶|

Back

Close

Full Screen / Esc

Printer-friendly Version

Interactive Discussion

It is clear that z_{desc} is unaffected by a El_{iceno} -variation and our strategy is that the terms $\alpha_{\text{atm}} \times z_{\text{atm}}$ and $\alpha_{\text{emit}} \times z_{\text{emit}}$ in the balance equation are modified. We keep the definitions of z_{atm} and z_{emit} and make the weights α_{atm} and α_{emit} dependent of El_{iceno} .

We define the normalised emission index $\text{El}_{\text{iceno}}^*$ as $\text{El}_{\text{iceno}}/\text{El}_{\text{iceno, ref}}$ and use a correction term of type $\text{El}_{\text{iceno}}^{*-y}$ for the weights. Then, the weights α_{atm} and α_{emit} are smaller for higher $\text{El}_{\text{iceno}}^*$. This reduces z_{Δ} and, correspondingly, \hat{f}_{Ns} becomes smaller, as desired.

Rows 4 and 5 shows the simulated survival fractions for a small El_{iceno} -variation for 6 AC types and a large El_{iceno} -variation for the default AC type. These subpanels demonstrate that the effect of an El_{iceno} -variation can be well captured by the corrected approximation. Note that without this correction the various symbols of a specific colour would all lie on one vertical line (i.e. identical z_{Δ}).

So far, the fuel flow changed only with AC type. As a last test, we vary the fuel flow (i.e. the WV emission \mathcal{V}) for a fixed AC type. The sensitivity simulations are listed in block 5 in Table A2 (originally discussed in Fig. 9 of U2014). Figure 11 nicely reveals that the sensitivity to \mathcal{V} is well represented in the parametrisation; for $\text{RH}_i = 110\%$ the agreement is excellent, for $\text{RH}_i = 120\%$ it is reasonable.

In the left panels, the vertical distance of the symbol (f_{Ns}) to the grey curve (\hat{f}) shows the absolute error $f_{\text{abs}} = \hat{f}_{\text{Ns}} - f_{\text{Ns}}$. In the right panels, scatter plots of \hat{f}_{Ns} vs. f_{Ns} are depicted and the errors can be more conveniently assessed. Furthermore, the root mean square of the absolute errors are given for each subset of simulations. The absolute errors are mostly below 0.1 for each subset, which proves the suitability of the proposed parametrisation.

S. Unterstrasser

[Title Page](#)[Abstract](#)[Introduction](#)[Conclusions](#)[References](#)[Tables](#)[Figures](#)[|◀](#)[▶|](#)[◀](#)[▶](#)[Back](#)[Close](#)[Full Screen / Esc](#)[Printer-friendly Version](#)[Interactive Discussion](#)

Finally, we provide the values of the fit parameters that were used for the computation of z_Δ and \hat{a} :

$$\beta_0 = 0.4 \quad (10a)$$

$$\beta_1 = 1.19 \quad (10b)$$

$$5 \quad \alpha_0 = -1.35 \quad (10c)$$

$$\alpha_{\text{atm}} = 1.7 \times EI_{\text{iceno}}^* e^{-\gamma_{\text{atm}}} \quad (10d)$$

$$\alpha_{\text{emit}} = 1.15 \times EI_{\text{iceno}}^* e^{-\gamma_{\text{emit}}} \quad (10e)$$

$$\alpha_{\text{desc}} = 0.6 \quad (10f)$$

$$\gamma_{\text{atm}} = 0.18 \quad (10g)$$

$$10 \quad \gamma_{\text{emit}} = 0.18 \quad (10h)$$

We determined these values by minimising the bias and standard deviation of the absolute and relative errors. Note that we did not apply a formal optimisation algorithm to find an optimal solution. We rather made a subjective trade-off between minimising the four error parameters.

15 Splitting the analysis into two separate length scales z_{atm} and z_{emit} , implicitly assumed linearity in e_s which is not the case. Using the combined length scale z_{buffer} defined by

$$(1 + s_i) \frac{e_s(T_{\text{CA}})}{R_v T_{\text{CA}}} + \rho_{\text{emit}} = \frac{e_s(T_{\text{CA}} + \Gamma_d z_{\text{buffer}})}{R_v (T_{\text{CA}} + \Gamma_d z_{\text{buffer}})} \quad (11)$$

may be more physically plausible and, indeed, z_{buffer} is up to 15% smaller than the sum of z_{atm} and z_{emit} . However, the main purpose is to design a parametrisation that approximates the simulated values the best. We found that the ansatz with two separate length scales allowed us to design a better parametrisation, as the weights α_{atm} and α_{emit} are individually adjustable.

25 The definitions of z_{atm} and z_{emit} (or z_{buffer}) rely on equating water vapour concentrations. One may argue that mixing ratios (and not concentrations) are conserved during

Title Page

Abstract

Introduction

Conclusions

References

Tables

Figures

|◀

▶|

◀

▶

Back

Close

Full Screen / Esc

Printer-friendly Version

Interactive Discussion

[Title Page](#)[Abstract](#)[Introduction](#)[Conclusions](#)[References](#)[Tables](#)[Figures](#)[|◀](#)[▶|](#)[◀](#)[▶|](#)[Back](#)[Close](#)[Full Screen / Esc](#)[Printer-friendly Version](#)[Interactive Discussion](#)

adiabatic processes. From this follows the conservation of $e_s(T)/T^\kappa$ with $\kappa = 3.5$ instead of $e_s(T)/T$.

As most of the variability in z_{atm} and z_{emit} comes from $e_s(T)$, using modified length scale definitions (with κ) would not improve the parametrisation.

5 3.3 Contrail depth

The determination of the contrail depth was exemplified in Sect. 2. Table A2 lists H -values for all simulations. Clearly, H depends on z_{desc} . The farther the vortices descend, the deeper the contrails can be (Fig. 2 right). On the other hand, the contrails may not reach the full vertical extent. In particular for slight supersaturations, the primary wake runs dry and all ice crystals in it are lost, as shown in Fig. 2 left. Thus, the parametrisation for H takes into account the combined effects of wake vortex descent and crystal loss.

Figure 6 left shows the relationship between H/\hat{z}_{desc} and \tilde{f}_{Ns} . Note that H is the contrail depth determined from the model simulations, whereas \hat{z}_{desc} and \tilde{f}_{Ns} are parametrisations (\tilde{f}_{Ns} is similar to \hat{f}_{Ns} and will be defined later). Using parametrised rather than simulated values for z_{desc} and f_{Ns} allows us to derive a parametrisation for H that is based only on available data. We suggest a piecewise linear function $\hat{b}(x)$ as an approximation for H/\hat{z}_{desc} as indicated by the grey curve.

Then the parametrised contrail height \hat{H} is given by:

$$20 \quad \hat{H} = \hat{z}_{\text{desc}} \times \hat{b}(\tilde{f}_{\text{Ns}}), \text{ where} \quad (12)$$

$$\hat{b}(x) = \begin{cases} \eta_1 x & x \in [0, x_s] \\ \eta_2 x + (\eta_1 - \eta_2) x_s & x \in [x_s, 1] \end{cases} \quad (13)$$

with $\eta_1 = 6, \eta_2 = 0.15$ and $x_s = 0.2$.

The piecewise definition reflects the fact, that contrail depth changes only slightly with large survival fractions and much stronger, once a major fraction of the ice crystals is

Properties of young contrails – a parametrisation based on large eddy simulations

S. Unterstrasser

[Title Page](#)

[Abstract](#)

[Introduction](#)

[Conclusions](#)

[References](#)

[Tables](#)

[Figures](#)

◀

▶

◀

▶

[Back](#)

[Close](#)

[Full Screen / Esc](#)

[Printer-friendly Version](#)

[Interactive Discussion](#)

lost. Thus, the definition is split into two parts (above and below x_s) and the slope of the approximation is much higher in the $x < x_s$ -part, i.e. η_1 is much larger than η_2 .

Note that \hat{b} can achieve values greater than unity implying that \hat{H} can be greater than \hat{z}_{desc} . This is reasonable as the contrail extends above the formation altitude on the one hand. Moreover, z_{desc} was determined by finding the centre of the primary wake whereas the contrail bottom is defined by the lower end of the plume.

Finally, we define \tilde{f}_{Ns} which is used in Eq. (12) and is in one aspect different from \hat{f}_{Ns} . Section 2 discussed that a variation of El_{iceno} has a small impact on the contrail mass and depth. The impact on crystal loss is however large and the values of \hat{f}_{Ns} are distributed over a large range, as can be seen in bottom right panel of Fig. 5. In the definition of \tilde{f}_{Ns} we exclude the El_{iceno} -effect by simple means. We take the original definition for \hat{f}_{Ns} and simply set $\gamma_{\text{atm}} = \gamma_{\text{emit}} = 0$. Then, \tilde{f}_{Ns} does not change with El_{iceno} . In rows 4 & 5 of Fig. 6 the various symbols of a specific colour all lie on one vertical line. From Eq. (12) follows that \hat{H} does not depend on El_{iceno} .

Analogous to Fig. 5, the right panel of Fig. 6 shows a scatter plot, now contrasting H vs. \hat{H} . Again, root mean squares of the absolute errors are supplied in the figure. They are below 50 m for each subset, which again proves the suitability of the proposed parametrisation.

3.4 Contrail width

Contrail width is a parameter whose choice is not as critical for the later evolution as that of contrail depth and ice crystal number. The horizontal spreading rate of a contrail is roughly given by $\dot{W} = H \times s$. For typical values $H = 400$ m and vertical wind shear $s = 0.005 \text{ s}^{-1}$ (considering only the component normal to contrail length axis), the width increases by 1 km every 8 min. Thus, an uncertainty in the initial width translates into a small offset in the assumed contrail age which becomes unimportant when looking at contrail-to-cirrus evolution over several hours.

The determination of the contrail width is based on the evaluation of transverse profiles of ice crystal mass after the vortex phase which are depicted in Fig. 7. The distri-

Title Page	
Abstract	Introduction
Conclusions	References
Tables	Figures
◀	▶
◀	▶
Back	Close
Full Screen / Esc	
Printer-friendly Version	
Interactive Discussion	

butions resemble roughly Gaussian distributions (at least in the absence of a sheared cross wind and when averaged along the flight direction).

For a B777-aircraft (left panel), most of the ice mass is confined to a 150 m broad band centered around the aircraft body. Towards the end of their lifetime, the vortex tubes meander and some ice is laterally even farther dislocated. This effect is not apparent, when all ice of the primary wake has been lost before this stage ($RH_i \leq 110\%$). The middle panel shows a modest dependence of contrail width on aircraft type. The smaller the aircraft wing span is, the smaller is the distance between the two vortex centers and exhaust plumes and the narrower is the final contrail. In the case with weaker stratification (right panel), the formation of vortex rings is pronounced, the vortex tubes oscillate more strongly and the contrail is broader.

3-D dynamical phenomena like the well-known Crow instability of the trailing vortices (Crow, 1970) lead to substantial variations along the flight direction, even if the environmental conditions are homogeneous in this direction, as exemplified by Lewellen et al. (1998); Unterstrasser et al. (2014) for conserved exhaust species and by Lewellen and Lewellen (2001); Unterstrasser (2014) for contrails.

This also implies that the contrail width varies along flight direction and attains its maximum values only in certain segments along the flight direction. Figure 8 depicts cross-sections of number concentrations from two slices, which are only 60 m apart. Slice B contains factor 2.5 more ice crystals than slice A. Moreover, the contrail is much broader, in particular in the lower part.

Global scale models, in which the current parametrisation might be employed in the future, cannot resolve such subtleties as contrail intrinsic heterogeneities. Thus, we propose the simple estimate $\hat{W} = 150\text{m}$ independent of the parameter settings. A more sophisticated approximation may include dependencies on wing span and Brunt–Väisälä frequency.

In global scale models, where the mean age of the initialised contrails is typically half the time step (which is at present times larger than the contrail age used here) one may correct for this offset in time.

If one is interested in deriving number concentrations from the parametrisations of N , H and W , a more suitable width parametrisation is presented in Sect. 4.3.

4 Applications

4.1 Test case of a soot reduction experiment

- 5 The number of generated ice crystals N_{form} depends on the number of emitted soot particles N_{soot} . The higher the corresponding emission indices are, the more crystals are lost during the vortex phase. We apply our derived parametrisation to determine an average survival rate for $\text{EI}_{\text{iceno}} = 10^{15}$, 10^{14} and 10^{13} kg^{-1} , respectively. The average is taken over a 4-D-cube varying relative humidity (100...140 %), temperature (210...226 K), Brunt–Väisälä frequency ($0.006\ldots0.014 \text{ s}^{-1}$) and wing span (20...84 m). Using the empirical relationships given by Eqs. (A5), (A9) and (A10), the wing span determines all relevant aircraft properties. For each parameter, the survival rate is evaluated for 9 values equally distributed over the given range (totaling 9^4 combinations). All data points are equally weighted, which could certainly be refined in the future.
- 15 About 29, 55 and 75 % of the ice crystal survive for $\text{EI}_{\text{iceno}} = 10^{15}$, 10^{14} and 10^{13} kg^{-1} . Thus, a EI_{iceno} -reduction from 10^{15} down to 10^{14} kg^{-1} (or 10^{14} down to 10^{13} kg^{-1}) implies “only” a factor 5.3 (or 7.4) reduction of the ice crystal number in the end. An initial factor 100 reduction gives 40 times fewer ice crystals in the end. Biofuels cause lower soot emissions with a likely impact on N_{form} . As the initial differences are reduced during the vortex phase, mitigation studies neglecting those effects may overestimate the effect of biofuels.

Title Page	
Abstract	Introduction
Conclusions	References
Tables	Figures
	
Back	Close
Full Screen / Esc	
Printer-friendly Version	
Interactive Discussion	

4.2 Sensitivity to input parameters

In this section, we analyse the sensitivity of N and H to the various input parameters of the parametrisation. We evaluate

$$\hat{N}_{\text{surv}} = N_{\text{form}} \times \hat{f}_{Ns} \quad (14)$$

- and \hat{H} for the 4-D-cube as defined above and take the average over 3 out of the 4 dimensions. Figure 9 shows the ice crystal number and the contrail depth after the vortex phase as a function of the various input parameters. We separate between scenarios with $El_{iceno} = 10^{15}$ and 10^{14} kg^{-1} . The variation in N is due to variations in N_{form} and \hat{f}_{Ns} . Note that N_{form} depends only on wing span b and El_{iceno} following Eq. (A10), whereas \hat{f}_{Ns} depends on all five parameters. In combination, we find that N depends most strongly on El_{iceno} and RH_i . A smaller impact have b , T_{CA} and N_{BV} (in this order).

The contrail depth depends most strongly on RH_i and b and to a lesser extent on T_{CA} and N_{BV} . According to the design of our parametrisation, the contrail depth does not depend on El_{iceno} .

- The sensitivity analyses reveal the most significant parameters for the determination of ice crystal number and contrail depth. It gives an estimate on how uncertainty in the input parameters translates into uncertainties in the output parameters.

Concerning the crystal loss determination, El_{iceno} and RH_i should be well characterised in some future application of the parametrisation, whereas for N_{BV} and T_{CA} it may be sufficient to have a rough estimate or to assume some default values.

4.3 Implications on number concentrations

From the parametrisations of N , H and W one may derive the mean ice crystal number concentration $\hat{n}_{\text{mean}} = \hat{N}_{\text{surv}} / (\hat{H} \hat{W})$ of a specific contrail. Hereby, we assume that the ice crystals are spread over a rectangular cross-section with width \hat{W} and height \hat{H} .

- Figure 10 contrasts \hat{n}_{mean} with the simulated values of n_{mean} . n_{mean} is given by N_{surv} / A ,

Title Page

Abstract

Introduction

Conclusions

References

Tables

Figures

|◀

▶|

◀

▶

Back

Close

Full Screen / Esc

Printer-friendly Version

Interactive Discussion

where A is the actual cross-sectional area of a contrail (averaged along flight direction). We find that \hat{n}_{mean} underestimates the simulated values by roughly a factor 5 (left panel). The main reason for this bias is that the parametrised area $\hat{A} = \hat{W} \hat{H}$ overestimates the real area A by around the same factor. In Fig. 8, the black boxes show the area-equivalent rectangle for this specific contrail with width $W_{\text{rect}} = A/H$. W_{rect} is much smaller than the actual width of the contrail. The parametrised number concentrations become more realistic, if we prescribe an “area-equivalent” width $W_{\text{rect}} = 0.63 b$ and use $\hat{A} = W_{\text{rect}} \hat{H}$ instead. The constant 0.63 is chosen such that the expectation value of $\Delta n_{\text{mean}} = \hat{n}_{\text{mean}} - n_{\text{mean}}$ is zero. The right panel 10 shows a much better agreement of \hat{n}_{mean} with n_{mean} . The standard deviation of the relative error $2 \Delta n_{\text{mean}} / (\hat{n}_{\text{mean}} + n_{\text{mean}})$ is around 50 %. The prediction of n_{mean} is more uncertain than that of N or H , as the uncertainties add together. The parametrised number concentrations are similarly realistic when we use $W_{\text{rect}} = 40 \text{ m}$ (not shown; again the expectation value is zero and the standard deviation is 55 %).

Depending on the purpose the parametrisation is applied for, we recommend to use either the \hat{W} -definition from Sect. 3.4 or the W_{rect} -definition from this section.

As the contrails get diluted, mean concentrations decrease over time. Evaluating the simulated n_{mean} at $t = 3 \text{ min}$ instead of at $t = 5 \text{ min}$, 1.65 ± 0.23 higher values are obtained.

Analogous to the analyses in Sect. 4.2, Fig. 9 middle shows the sensitivity of \hat{n}_{mean} (after 5 min) to the various input parameters of the parametrisation. We find a dominant impact of EI_{iceno} and RH_i . b , T_{CA} and N_{BV} appear to be less important. Using $W_{\text{rect}} = 36 \text{ m}$ instead of $W_{\text{rect}} = 0.63 b$, various opposing trends do not cancel out and the sensitivity to b is larger (not shown).

Deriving analogous relations for ice water content or optical depth would be desirable. As we do not parametrise the contrail ice mass, this cannot be achieved with the present parametrisation.

Title Page	Abstract	Introduction
Conclusions	References	
Tables	Figures	
◀	▶	
◀	▶	
Back	Close	
Full Screen / Esc		
Printer-friendly Version		
Interactive Discussion		

5 Discussion

In the preceding section we introduced parametrisations of crystal loss and contrail depth which take into account the effect of the most important parameters, namely temperature at cruise altitude T_{CA} , ambient relative humidity RH_i , Brunt–Väisälä frequency N_{BV} , aircraft properties (defining the initial wake vortex properties and the water vapour emission) and ice crystal “emission” index El_{iceno} .

5.1 Further sensitivities

Several further parameters may affect the early contrail evolution. Their importance, which have been partly investigated by recent 3-D simulation studies, will be discussed in the following.

Stronger vertical wind shear and higher ambient turbulence potentially speed up the vortex decay. However, for stratification values typical of the upper troposphere, variations of vertical wind shear s (assuming a linear wind profile) and turbulence are second order effects and wake vortex descent, contrail height and crystal loss are fairly unaffected by such variations (Huebsch and Lewellen, 2006; Hennemann and Holzäpfel, 2011; Naiman et al., 2011; Unterstrasser et al., 2014; Picot et al., 2015). For strongly curved wind profiles (i.e. non-zero \dot{s}) vortex decay may be accelerated and the situation becomes more intricate.

Cruise altitude mainly determines the ambient temperature, pressure and air density (linked by the ideal gas law). Note that the definition of z_{atm} and z_{emit} are based on equating water vapour concentrations which do not depend on ambient pressure/density (unlike to mixing ratios). Thus the contrail ice mass balance and consequently crystal loss and contrail depth are in theory not affected by ambient pressure. Ambient pressure affects, e.g., the diffusivity of water vapour and thus ice crystal growth (Ghosh et al., 2007; Pruppacher and Klett, 1997). But the sensitivity is too weak to be important in this case as confirmed by 2-D contrail simulations (Unterstraßer, 2008).

Title Page

Abstract

Introduction

Conclusions

References

Tables

Figures

|◀

▶|

◀

▶

Back

Close

Full Screen / Esc

Printer-friendly Version

Interactive Discussion

Note that the variation of other microphysical constants (not dependent on pressure) like the deposition coefficient induce larger uncertainties (Lewellen et al., 2014).

The initial circulation Γ_0 of the wake vortices is inversely proportional to the air density (see Eq. A1) and changes with flight altitude. Compared to the variation of aircraft mass and wing span, the rather small changes in ρ_{air} have a second order effect on Γ_0 and the wake vortex displacement z_{desc} . Thus, the dependence of contrail evolution on flight altitude is mainly a temperature effect.

In the simulations presented in Sect. 3 ambient relative humidity was assumed to be uniform over the entire domain. Hence, we do not cover scenarios with a thin supersaturated layer where the contrail leaves the supersaturated layer at some point during the wake vortex descent. A thin moist layer may limit the contrail depth and inhibit contrail growth in its early stage. However such scenarios have not yet been analysed in any LES study of young contrails. So far, the impact of the depth of the supersaturated layer was only investigated for contrail-cirrus (Unterstrasser and Gierens, 2010b; Lewellen, 2014), i.e the supersaturated layer was deep enough to contain the young contrail, yet limited the later formation of the fall streak.

All simulations discussed in Sect. 3 use the standard configuration, as we call it. Further uncertainties arise from the choice of this configuration and may have an impact on the simulated crystal loss and contrail depth. Clearly, these parameters are not reflected in our parametrisations. This includes variations of the spatial initialisation and the initial width of the ice crystal size distribution as well as the disregard of the Kelvin effect in the ice growth equation. Their effects have been discussed in detail in U2014 and the effect on contrail depth was found to be negligible and is not further discussed here. Crystal loss, however, is affected and in the following we discuss whether this downgrades the universality of our parametrisations.

Figure 11 depicts f_{Ns} of these sensitivity simulations (coloured symbols) and contrasts them with the simulations with the standard configuration (grey symbols, all simulations were originally depicted in Fig. 5).

Title Page	
Abstract	Introduction
Conclusions	References
Tables	Figures
	
Back	Close
Full Screen / Esc	
Printer-friendly Version	
Interactive Discussion	

[Title Page](#)[Abstract](#)[Introduction](#)[Conclusions](#)[References](#)[Tables](#)[Figures](#)[|](#)[|](#)[◀](#)[▶](#)[Back](#)[Close](#)[Full Screen / Esc](#)[Printer-friendly Version](#)[Interactive Discussion](#)

In the default configuration, UG2014 and U2014 use a simple spatial initialisation, i.e. the crystal number concentrations are constant inside the two initial plumes. Following the approach of Lewellen et al. (2014) and Naiman et al. (2011), Gaussian-like distributions of ice crystal number concentrations were alternatively prescribed (see blue symbols). The effect on the crystal loss extent was often low (originally discussed in Fig. 7 in UG2014). In one particular case with high temperature and relative humidity, the crystal loss was stronger, once a Gaussian distribution was used (originally discussed in Fig. 13 of U2014, blue square in our Fig. 11). If a Gaussian distribution is more realistic, the survival rates may be overestimated for high supersaturations.

Based on the assumption of spherical ice crystals, the standard configuration includes a correction of the local relative humidity over a curved surface (Kelvin effect) in the ice crystal growth equation. It is not clear how physically plausible this is, as ice crystals are never perfect spheres. When we switch off the Kelvin correction, fewer ice crystals are lost (brown symbols), as expected.

In U2014, the initial width of the ice crystal size distribution was varied, as it cannot be measured or numerically determined accurately enough (see discussion in Unterstrasser and Söhlch, 2010). The narrower the SD is chosen, the fewer ice crystals are lost (green symbols). Note that Lewellen et al. (2014) reports a weaker sensitivity to this parameter which may be connected to the fact that the spatial initialisation of the ice crystals and the assumed initial wake age differ between their study and ours.

Ideally, the initialisation of the vortex phase simulations would use input from 3-D jet phase simulations that model the contrail formation with a detailed ice activation scheme and which could provide 3-D fields of the ice crystal size distribution, water vapour, temperature and velocity (only to name the most important ones). Unfortunately, such simulations are not available. Up to date, 3-D jet phase simulations employ simplified ice activation schemes (Paoli et al., 2004, 2013; Garnier et al., 2014), whereas detailed plume microphysics are embedded in 0-D-models with prescribed plume dilution (Kärcher and Yu, 2009; Yu and Turco, 1998).

Overall, we can state that the “new” data points (of the sensitivity simulations) lie within the spread of data points with the standard configuration. This implies that the uncertainties/biases due to the numerical configuration are smaller than the deviations of the simulation results from the fit function. This suggests that the uncertainties are acceptable given the accuracy of the parametrisation.

5.2 Comparison with other LES models

The early contrail evolution has been studied by several groups with different LES codes in the past (Huebsch and Lewellen, 2006; Lewellen et al., 2014; Naiman et al., 2011; Paugam et al., 2010; Picot et al., 2015). Qualitatively, the sensitivity trends are similar for most studies (except for one outlier model discussed below) and confirms the reliability of the model results. Nevertheless, quantitative comparisons between the various models were always hampered by the fact that in each study parameter variations started from different base states. This means that differences in the simulated contrail properties could always be attributed to slightly different input parameters and as a consequence possible systematic differences may be overlooked. Our approach offers an ideal framework to make a more in-depth intercomparison between the models and further check whether the results from other LES models support our proposed parametrisation. Table A2 lists input parameters as well as the values for f_{Ns} and H from several simulations of the above mentioned studies. Analogous to the evaluation in Sect. 3, we compute z_Δ and \hat{z}_{desc} for the given input parameters and derive the approximated values for the survival fraction and contrail depth. Those are then compared to the simulated values (see Fig. 12). First we discuss the survival rates depicted in the top row. All EULAG-LCM results from UG2014 and U2014 are plotted as light grey symbols; results from other groups are plotted with coloured symbols. The data set includes a combined variation of T_{CA} and RH_i (red crosses) as well as a wide range EI_{iceno} -variation (red plus symbols) by Lewellen et al. (2014). We find that their simulated values for the survival fraction nicely follows our parametrisation, i.e. the red symbols are not farther away from the 1-to-1 line (in the right hand side panel) than

[Title Page](#)[Abstract](#)[Introduction](#)[Conclusions](#)[References](#)[Tables](#)[Figures](#)[|◀](#)[▶|](#)[◀](#)[▶](#)[Back](#)[Close](#)[Full Screen / Esc](#)[Printer-friendly Version](#)[Interactive Discussion](#)

the grey symbols. Similarly, the few data points by Picot et al. (2015) agree reasonably well with our parametrisation. This demonstrates the consistency between those models and also the robustness of the f_{Ns} -parametrisation. Now we turn our attention to the survival rates simulated by Naiman et al. (2011) (brown diamonds). Unterstrasser (2014, their Sect. 3.5) already pointed out that the observed trends in several sensitivity studies of Naiman et al. (2011) disagreed with all other models and appeared implausible. The present analysis confirms this and reveals an inconsistency of their data with our f_{Ns} -parametrisation. Obviously, their survival rates scatter strongly and there is no correlation between their f_{Ns} -values and the predicted values \hat{f}_{Ns} .

As a next step, we compare the contrail depth values of the various models (bottom row of Fig. 12). Again, the data points from the other groups are added in colour. From Picot et al. (2015) (green squares) and Huebsch and Lewellen (2006) (red crosses), H values are available for $RH_i = 130\%$ and $RH_i = 110\%$ -simulations. For the other studies, only results of $RH_i = 130\%$ simulations are available. For all $RH_i = 130\%$ -cases, the contrails reach their full vertical extent and accordingly the ratio H/\hat{z}_{desc} is around 1.2–1.4 (left panel) as in our EULAG-LCM simulations. For the $RH_i = 110\%$ -simulations, contrail depth H is smaller as already observed in our EULAG-LCM simulations. The left panel reveals that the “new” H -values support the piecewise linear approximation. The right panel shows non-normalised values of H and focuses on the variations in z_{desc} . In particular, the H -values of three different aircraft types in Naiman et al. (2011) (brown diamonds) are useful for comparison, as the wake vortex descent and with it the contrail depth vary over a wide range. Apparently, all H -values are close to the 1-to-1 line which leads to the conclusion that the wake vortex descent is strikingly similar in all models.

25 5.3 Comparison with observations

Young contrails have been measured in-situ or with lidars in the past. Unfortunately, total ice crystal number cannot reliably be determined with those methods. Lidars do not measure ice crystal numbers and in-situ measurements do not sample the com-

Properties of young contrails – a parametrisation based on large eddy simulations

S. Unterstrasser

[Title Page](#)

[Abstract](#)

[Introduction](#)

[Conclusions](#)

[References](#)

[Tables](#)

[Figures](#)

[|◀](#)

[▶|](#)

[◀](#)

[▶](#)

[Back](#)

[Close](#)

[Full Screen / Esc](#)

[Printer-friendly Version](#)

[Interactive Discussion](#)



plete contrail which would be necessary to derive such an integral property. Thus, we limit ourselves to compare the contrail depth with lidar measurements and ice crystal number concentrations with in-situ measurements. We have seen that contrail properties depend on a multitude of parameters and usually not all them are determined with sufficient accuracy to evaluate our proposed parametrisation. Moreover, contrails are heterogeneous and in-situ measured properties may depend on how and where the contrail is sampled. As an example for the contrail heterogeneity, Fig. 13 shows the occurrence frequencies of ice crystal number concentrations inside specific 3 and 5 min old contrails. Having in mind all the above arguments, it is clear that the following exercise can only serve as general sanity check.

Freudenthaler et al. (1995) used a ground based lidar and finds the heights of a few young contrails to range between 150 m and 300 m. We hypothesise that the contrails were produced from small to medium sized aircraft, in modestly supersaturated or stratified environments as their values do not reach our maximum values. In-situ measurements of number concentrations (Voigt et al., 2011; Kaufmann et al., 2014) show mean values of around 100–200 cm³ consistent with our data.

6 Conclusions

Based on the evaluation of a large data set of large eddy simulations (LES) of young contrails, we derived analytical approximations of contrail depth and ice crystal number for 5 min old contrails. At that time, the wake vortices decayed and related important aircraft induced effects, which affect the contrail depth and crystal loss in the primary wake, ceased. The parametrisation may be implemented in contrail models that do not explicitly resolve the wake dynamics and where the contrail initialisation refers to some state after vortex breakup.

The proposed parametrisation captures the fundamental microphysical and dynamical processes in a young contrail. It takes into account the impact of ambient relative humidity RH_i, temperature T_{CA} (at cruise altitude), thermal stratification specified by

[Title Page](#)[Abstract](#)[Introduction](#)[Conclusions](#)[References](#)[Tables](#)[Figures](#)[|◀](#)[▶|](#)[Back](#)[Close](#)[Full Screen / Esc](#)[Printer-friendly Version](#)[Interactive Discussion](#)

the Brunt–Väisälä frequency N_{BV} , ice crystal “emission” index EI_{iceno} and aircraft parameters. The latter are the water vapour emission \mathcal{V} , the wing span b and the initial circulation Γ_0 of the wake vortex. If aircraft properties are not available, empirical relationships $\mathcal{V}(b)$ and $\Gamma_0(b)$ are provided such that only wing span b must be specified.

We find that, on average, the ice crystal number N depends most sensitively on EI_{iceno} and RH_i and to a lesser extent on b , T_{CA} and N_{BV} (in this order). For the contrail depth H , RH_i and b are most significant followed by T_{CA} and N_{BV} . Contrail depth is independent of EI_{iceno} (according to the design of our parametrisation).

For the contrail width, we recommend a value of $W = 150\text{m}$. The contrail cross-section is far from having a rectangular shape and the simple estimate $W \times H$ overestimates the contrail cross-sectional area A by up to a factor 5. This has to be taken into account if number concentrations $n = N/A$ are derived from the parametrisation.

For persistent contrails, the ranges of typical N , H and n -values are 10^{11} to 10^{13} m^{-1} , 100 to 600 m and 10 to several hundred cm^3 , respectively.

The parametrisation offers an ideal framework to compare simulation results from various LES models. We find an excellent agreement regarding the contrail depth and good agreement regarding the crystal number. This demonstrates the robustness of the proposed parametrisation.

A EI_{iceno} -reduction from 10^{15} down to 10^{14} kg^{-1} (or 10^{14} down to 10^{13} kg^{-1}) implies “only” a factor 5.3 (or 7.4) reduction of the ice crystal number in the end. An initial factor 100 reduction (from 10^{15} down to 10^{13} kg^{-1}) gives 40 times fewer ice crystals in the end. Biofuels have lower soot emissions with a likely impact on the number of generated ice crystals. As the initial differences are reduced during the vortex phase, mitigation studies neglecting those effects may overestimate the effect of biofuels.

Properties of young contrails – a parametrisation based on large eddy simulations

S. Unterstrasser

[Title Page](#)

[Abstract](#)

[Introduction](#)

[Conclusions](#)

[References](#)

[Tables](#)

[Figures](#)

[◀](#)

[▶](#)

[Back](#)

[Close](#)

[Full Screen / Esc](#)

[Printer-friendly Version](#)

[Interactive Discussion](#)



A1 Wake vortex

The initial circulation of the wake vortices is given by

$$\Gamma_0 = \frac{g M}{\rho_{\text{air}} b_0 U}, \quad (\text{A1})$$

- where g is the gravity constant, M is the aircraft mass, U the cruise speed (around 230 m s^{-1}) and ρ_{air} the density of air (around 0.4 kg m^{-3}).

The initial vortex separation b_0 is

$$b_0 = \frac{\pi}{4} b, \quad (\text{A2})$$

where b is the wing span. As the two vortices are counter-rotating, one vortex has positive sign and the other one negative sign.

The initial descent of the wake vortex pair is given by

$$w_0 = \frac{\Gamma_0}{2\pi b_0}. \quad (\text{A3})$$

A2 Vertical displacement

In wake vortex research, it is common to use equations and analyse results in non-dimensional form (Gerz et al., 2002). For this, the following scaling parameters are used: length scale b_0 , velocity scale w_0 and time scale $t_0 = b_0/w_0$. Values of w_0 and t_0 for the various aircraft types are listed in Table 1.

In UG2014, the non-dimensional form was useful to find a simple parametrisation of the vertical displacement $z_{\text{desc}}^* = z_{\text{desc}}/b_0$ in terms of normalised Brunt–Väisälä frequency $N_{\text{BV}}^* = N_{\text{BV}} \times t_0$ (see their Fig. 8 and Eq. 7). Stepping back to the dimensional

Properties of young contrails – a parametrisation based on large eddy simulations

S. Unterstrasser

[Title Page](#)

[Abstract](#)

[Introduction](#)

[Conclusions](#)

[References](#)

[Tables](#)

[Figures](#)

[|◀](#)

[▶|](#)

[◀](#)

[▶](#)

[Back](#)

[Close](#)

[Full Screen / Esc](#)

[Printer-friendly Version](#)

[Interactive Discussion](#)



form (their Eq. 8), the vertical displacement is then given by

$$\hat{z}_{\text{desc}} = \alpha' b_0^{(1-2\beta)} \Gamma_0^\beta N_{\text{BV}}^{-\beta}. \quad (\text{A4})$$

For the reasonable fit parameter $\beta = 0.5$, b_0 drops out in Eq. (A4), and \hat{z}_{desc} depends solely on Γ_0 and N_{BV} , as given in Eq. (4).

- 5 In case, information on Γ_0 is not available, Sect. A3 proposes a simple relationship between Γ_0 and wing span.

A3 Circulation estimate

It is well conceivable, that the parameter Γ_0 is not available in typical applications of the parametrisations. Ignoring the fact that the aircraft mass and circulation (see

- 10 Eq. A1) change with time and kerosene loading, we propose the following simplification: Fig. A1a shows the relationship between wing span and initial circulation as used in UG2014. There, the initial circulation was computed assuming a medium aircraft mass (between empty aircraft and maximum takeoff mass taken from the BADA data set). Then, the crude relationship

$$15 \quad \Gamma_0 = (-70 \text{ m} + 10b) \text{ ms}^{-1} \quad (\text{A5})$$

holds, which can be plugged into Eq. (4).

Note that from a physical point of view, it is counter-intuitive to integrate b into an approximation of \hat{z}_{desc} as it originally dropped out stepping from Eq. (A4) to Eq. (4).

A4 Plume area

- 20 For the computation of z_{emit} it is important to know over which area (normal to the flight direction) the ice crystals in the primary wake are distributed. Looking at cross-sections of the plume we manually determine its radius r_p at some intermediate stage. The r_p -values are depicted in Fig. A1b and are roughly linearly dependent on wing

[Title Page](#)
[Abstract](#)
[Introduction](#)
[Conclusions](#)
[References](#)
[Tables](#)
[Figures](#)
[|◀](#)
[▶|](#)
[Back](#)
[Close](#)
[Full Screen / Esc](#)
[Printer-friendly Version](#)
[Interactive Discussion](#)


span b :

$$r_p = 1.5 \text{ m} + 0.314 b \quad (\text{A6})$$

The area of the two plumes is given by

$$A_p = 2 \times 2\pi r_p^2 \quad (\text{A7})$$

- and thus scales roughly with b^2 . It is clear that once the vortices strongly oscillate, link or break up, the determination of r_p it not meaningful any longer. For each aircraft, we ran a sensitivity simulation where we increased the radius R_{init} of the initial plume (Sect. 3.4 of UG2014). We find the intermediate plume radius r_p (star symbol) to be independent of the initial setting and to lie in between of the two initial values (diamond symbol).

A5 Water vapour emission

The water vapour emission is given by

$$\mathcal{V} = \frac{\dot{m}_f}{U} \text{ EI}_{H20}, \quad (\text{A8})$$

- UG2014 assumed a medium fuel flow representative of cruise conditions (again based on BADA data). Figure A1c suggests that \mathcal{V} scales with b^2 . The fit function is given by

$$\mathcal{V} = 0.020 \text{ kg m}^{-1} (b/80 \text{ m})^2 \quad (\text{A9})$$

Combining Eqs. (2), (A8) and (A9) we can estimate the number of generated ice crystals by

$$N_{\text{form}} = \text{EI}_{\text{iceno}} \times 0.0160 \text{ kg m}^{-1} (b/80 \text{ m})^2. \quad (\text{A10})$$

Title Page	
Abstract	Introduction
Conclusions	References
Tables	Figures
◀	▶
◀	▶
Back	Close
Full Screen / Esc	
Printer-friendly Version	
Interactive Discussion	

A6 Mode of use

This section gives a summary on the presented parametrisations and deals with their computation. Note that the Supplement contains a Fortran programme for the computation of \hat{f}_{Ns} and \hat{H} .

5 The following input parameters have to be known:

- temperature at cruise altitude T_{CA}
- ambient relative humidity RH_i
- Brunt–Väisälä frequency N_{BV}
- wing span of the aircraft b
- ice crystal “emission” index EI_{iceno}
- optionally: aircraft mass
- optionally: fuel flow of the aircraft (total of all engines)

10 Steps for computation of \hat{f}_{Ns} :

- 15 1. Compute Γ_0 with Eq. (A1) and \hat{z}_{desc} with Eq. (4). If data on the aircraft mass are not available, use the relationship given in Eq. (A5) to compute Γ_0 .
2. Compute the concentration add-on ρ_{emit} using Eqs. (6), (A7) and (A8). If data on the fuel flow are not available, use the relationship given in Eq. (A9).
3. Compute z_{atm} and z_{emit} via solving the non-linear Eqs. (5) and (7).
4. Compute z_Δ with Eq. (3) and the fit parameters given in Eqs. (10d)–(10h).
- 20 5. Compute \hat{f}_{Ns} with Eqs. (8) and (9) and fit parameters given in Eqs. (10a)–(10c).

Title Page	
Abstract	Introduction
Conclusions	References
Tables	Figures
◀	▶
◀	▶
Back	Close
Full Screen / Esc	
Printer-friendly Version	
Interactive Discussion	

6. The total ice crystal number \hat{N} is given by Eq. (14). If data on the fuel flow are not available, use the relationship given in Eq. (A10) instead of Eq. (2).

Steps for computation of \hat{H} :

1. Steps 1–3 as above.
- 5 2. Compute z_Δ with Eq. (3) and the fit parameters given in Eqs. (10d)–(10f) and $\gamma_{\text{atm}} = \gamma_{\text{emit}} = 0$.
3. Compute \tilde{f}_{Ns} with Eqs. (8) and (9) and fit parameters given in Eqs. (10a)–(10c).
4. Compute \hat{H} with Eqs. (12) and (13).

The Supplement related to this article is available online at
10 doi:10.5194/acpd-15-28939-2015-supplement.

Acknowledgements. The author is partly funded by the DFG (German Science Foundation, contract number UN286/1–2). Computational resources were made available by the German Climate Computing Center (DKRZ) through support from the German Federal Ministry of Education and Research (BMBF). I thank my former student N. Görsch for preparatory work
15 and several DLR colleagues for discussions. I am indebted to D. Lewellen and R. Paoli who provided me with their simulation data.

The article processing charges for this open-access publication were covered by a Research Centre of the Helmholtz Association.

20 References

Boucher, O., Randall, D., Artaxo, P., Bretherton, C., Feingold, G., Forster, P., Kerminen, V.-M., Kondo, Y., Liao, H., Lohmann, U., Rasch, P., Satheesh, S., Sherwood, S., Stevens, B.,

[Title Page](#)

[Abstract](#)

[Introduction](#)

[Conclusions](#)

[References](#)

[Tables](#)

[Figures](#)

◀

▶

[Back](#)

[Close](#)

[Full Screen / Esc](#)

[Printer-friendly Version](#)

[Interactive Discussion](#)



- and Zhang, X.: Clouds and Aerosols, book section 7, 571–658, Cambridge University Press, Cambridge, UK and NY, USA, doi:10.1017/CBO9781107415324.016, 2013. 28940
- Burkhardt, U. and Kärcher, B.: Process-based simulation of contrail cirrus in a global climate model, *J. Geophys. Res.*, 114, D16201, doi:10.1029/2008JD011491, 2009. 28941
- 5 Burkhardt, U. and Kärcher, B.: Global radiative forcing from contrail cirrus, *Nature Climate Change*, 1, 54–58, 2011. 28940
- Chen, C.-C. and Gettelman, A.: Simulated radiative forcing from contrails and contrail cirrus, *Atmos. Chem. Phys.*, 13, 12525–12536, doi:10.5194/acp-13-12525-2013, 2013. 28941
- Crow, S.: Stability theory for a pair of trailing vortices, *AIAA J.*, 8, 2172–2179, 1970. 28957
- 10 Freudenthaler, V., Homburg, F., and Jäger, H.: Contrail observations by ground-based scanning lidar: Cross-sectional growth, *Geophys. Res. Lett.*, 22, 3501–3504, 1995. 28966
- Garnier, F., Maglaras, E., Morency, F., and Vancassel, X.: Effect of Compressibility on Contrail Ice Particle Growth in an Engine Jet, *Int. J. Turbo. Jet. Eng.*, 31, 131–140, 2014. 28963
- 15 Gerz, T., Holzapfel, F., and Darracq, D.: Commercial aircraft wake vortices, *Prog. Aerosp. Sci.*, 38, 181–208, 2002. 28968
- Ghosh, S., Dobbie, S., Marsham, J., and Jonas, P.: On the importance of the diffusional uptake of water vapour for the development and radiative properties of high altitude clouds: a large eddy model sensitivity study, *Q. J. Roy. Meteor. Soc.*, 133, 1731–1741, 2007. 28961
- Hennemann, I. and Holzapfel, F.: Large-eddy simulation of aircraft wake vortex deformation and topology, *P. I. Mech. Eng. G-J. Aer.*, 225, 1336–1350, doi:10.1177/0954410011402257, 2011. 28961
- 20 Hoshizaki, H., Anderson, L. B., Conti, R. J., Farlow, N., Meyer, J. W., Overcamp, T., Redler, K. O., and Watson, V.: Aircraft Wake Microscale Phenomena, in: The Stratosphere perturbed by Propulsion Effluents, U. S. Dep. of Transportation DOT-TST-75-53, Washington, D. C., USA, 1975. 28942
- Huebsch, W. and Lewellen, D.: Sensitivity Study on Contrail Evolution, 36th AIAA Fluid Dynamics Conference and Exhibit, 5–8 June 2006, San Francisco, USA, AIAA 2006-3749, 1–14, <http://arc.aiaa.org/doi/pdfplus/10.2514/6.2006-3749>, 2006. 28961, 28964, 28965, 28982
- 25 Kärcher, B. and Yu, F.: Role of aircraft soot emissions in contrail formation, *Geophys. Res. Lett.*, 36, L01804, doi:10.1029/2008GL036649, 2009. 28942, 28944, 28963, 28984
- Kärcher, B., Busen, R., Petzold, A., Schröder, F. P., Schumann, U., and Jensen, E. J.: Physicochemistry of aircraft-generated liquid aerosols, soot, and ice particles. 2. Comparison with observations and sensitivity studies, *J. Geophys. Res.*, 103, 17129–17148, 1998. 28944

Properties of young contrails – a parametrisation based on large eddy simulations

S. Unterstrasser

[Title Page](#)

[Abstract](#)

[Introduction](#)

[Conclusions](#)

[References](#)

[Tables](#)

[Figures](#)

[◀](#)

[▶](#)

[◀](#)

[▶](#)

[Back](#)

[Close](#)

[Full Screen / Esc](#)

[Printer-friendly Version](#)

[Interactive Discussion](#)



Properties of young contrails – a parametrisation based on large eddy simulations

S. Unterstrasser

[Title Page](#)

[Abstract](#)

[Introduction](#)

[Conclusions](#)

[References](#)

[Tables](#)

[Figures](#)

[|◀](#)

[▶|](#)

[◀](#)

[▶](#)

[Back](#)

[Close](#)

[Full Screen / Esc](#)

[Printer-friendly Version](#)

[Interactive Discussion](#)

Kärcher, B., Burkhardt, U., Unterstrasser, S., and Minnis, P.: Factors controlling contrail cirrus optical depth, *Atmos. Chem. Phys.*, 9, 6229–6254, doi:10.5194/acp-9-6229-2009, 2009. 28941

Kaufmann, S., Voigt, C., Jeßberger, P., Jurkat, T., Schlager, H., Schwarzenboeck, A., Klingebiel, M., and Thornberry, T.: In situ measurements of ice saturation in young contrails, *Geophys. Res. Lett.*, 41, 702–709, doi:10.1002/2013GL058276, 2014. 28966

Lewellen, D. and Lewellen, W.: The effects of aircraft wake dynamics on contrail development, *J. Atmos. Sci.*, 58, 390–406, 2001. 28957

Lewellen, D., Lewellen, W., Poole, L., DeCoursey, R., Hansen, G., Hostetler, C., and Kent, G.: Large-eddy simulations and lidar measurements of vortex-pair breakup in aircraft wakes, *AIAA J.*, 36, 1439–1445, 1998. 28957

Lewellen, D. C.: Persistent contrails and contrail cirrus. Part 2: Full Lifetime Behavior, *J. Atmos. Sci.*, 71, 4420–4438, doi:10.1175/JAS-D-13-0317.1, 2014. 28941, 28942, 28943, 28962

Lewellen, D. C., Meza, O., and Huebsch, W. W.: Persistent contrails and contrail cirrus. Part 1: Large-eddy simulations from inception to demise, *J. Atmos. Sci.*, 71, 4399–4419, doi:10.1175/JAS-D-13-0316.1, 2014. 28943, 28962, 28963, 28964, 28982, 28995

Naiman, A. D., Lele, S. K., and Jacobsen, M. Z.: Large eddy simulations of contrail development: Sensitivity to initial and ambient conditions over first twenty minutes, *J. Geophys. Res.*, 116, D21208, doi:10.1029/2011JD015806, 2011. 28961, 28963, 28964, 28965, 28977, 28983, 28995

Nuic, A.: User manual for the Base of Aircraft Data (BADA), Revision 3.9, Tech. rep., EEC Technical/Scientific Report No. 11/03/08-08, EUROCONTROL, Bruxelles, Belgium, 2011. 28946

Paoli, R., Hélie, J., and Poinsot, T.: Contrail formation in aircraft wakes, *J. Fluid Mech.*, 502, 361–373, 2004. 28963

Paoli, R., Nybelen, L., Picot, J., and Cariolle, D.: Effects of jet/vortex interaction on contrail formation in supersaturated conditions, *Phys. Fluids*, 25, 1–28, 2013. 28942, 28963

Paugam, R., Paoli, R., and Cariolle, D.: Influence of vortex dynamics and atmospheric turbulence on the early evolution of a contrail, *Atmos. Chem. Phys.*, 10, 3933–3952, doi:10.5194/acp-10-3933-2010, 2010. 28964, 28977, 28983, 28995

Picot, J., Paoli, R., Thouron, O., and Cariolle, D.: Large-eddy simulation of contrail evolution in the vortex phase and its interaction with atmospheric turbulence, *Atmos. Chem. Phys.*,

Properties of young contrails – a parametrisation based on large eddy simulations

S. Unterstrasser

- 15, 7369–7389, doi:10.5194/acp-15-7369-2015, 2015. 28961, 28964, 28965, 28977, 28983,
28995
- Ponater, M., Marquart, S., and Sausen, R.: Contrails in a comprehensive global climate model: Parameterization and radiative forcing results, *J. Geophys. Res.*, 107, 941–960, 2002. 28941
- Pruppacher, H. and Klett, J.: *Microphysics of clouds and precipitation*, Kluwer Acad. Pub., Dordrecht, the Netherlands, 1997. 28961
- Rap, A., Forster, P., Jones, A., Boucher, O., Haywood, J., Bellouin, N., and De Leon, R.: Parameterization of contrails in the UK Met Office Climate Model, *J. Geophys. Res.*, 115, D10205, doi:10.1029/2009JD012443, 2010. 28941
- Schumann, U.: On conditions for contrail formation from aircraft exhausts, *Meteorol. Z.*, 5, 4–23, 1996. 28942
- Schumann, U.: A contrail cirrus prediction model, *Geosci. Model Dev.*, 5, 543–580, doi:10.5194/gmd-5-543-2012, 2012. 28941
- Sölich, I. and Kärcher, B.: A large-eddy model for cirrus clouds with explicit aerosol and ice microphysics and Lagrangian ice particle tracking, *Q. J. Roy. Meteor. Soc.*, 136, 2074–2093, 2010. 28944
- Süssmann, R. and Gierens, K.: Lidar and numerical studies on the different evolution of vortex pair and secondary wake in young contrails, *J. Geophys. Res.*, 104, 2131–2142, 1999. 28942
- Untersträßer, S.: Numerische Simulationen von Kondensstreifen und deren Übergang in Zirren, PhD thesis, LMU München, Germany, 2008. 28961
- Untersträßer, S.: Large eddy simulation study of contrail microphysics and geometry during the vortex phase and consequences on contrail-to-cirrus transition, *J. Geophys. Res.*, 119, 7537–7555, doi:10.1002/2013JD021418, 2014. 28941, 28943, 28944, 28945, 28957, 28965
- Untersträßer, S. and Gierens, K.: Numerical simulations of contrail-to-cirrus transition – Part 1: An extensive parametric study, *Atmos. Chem. Phys.*, 10, 2017–2036, doi:10.5194/acp-10-2017-2010, 2010a. 28943
- Untersträßer, S. and Gierens, K.: Numerical simulations of contrail-to-cirrus transition – Part 2: Impact of initial ice crystal number, radiation, stratification, secondary nucleation and layer depth, *Atmos. Chem. Phys.*, 10, 2037–2051, doi:10.5194/acp-10-2037-2010, 2010b. 28943, 28962
- Untersträßer, S. and Görsch, N.: Aircraft-type dependency of contrail evolution, *J. Geophys. Res.*, 119, 14015–14027, doi:10.1002/2014JD022642, 2014. 28941, 28943, 28944, 28945

Discussion Paper | Discussion Paper

Discussion Paper | Discussion Paper

Discussion Paper | Discussion Paper

Title Page	
Abstract	Introduction
Conclusions	References
Tables	Figures
	
	
Full Screen / Esc	
Printer-friendly Version	
Interactive Discussion	

**Properties of young
contrails –
a parametrisation
based on large eddy
simulations**

S. Unterstrasser

[Title Page](#)[Abstract](#)[Introduction](#)[Conclusions](#)[References](#)[Tables](#)[Figures](#)[|](#)[|](#)[◀](#)[▶](#)[Back](#)[Close](#)[Full Screen / Esc](#)[Printer-friendly Version](#)[Interactive Discussion](#)

Unterstrasser, S. and Söhlch, I.: Study of contrail microphysics in the vortex phase with a Lagrangian particle tracking model, *Atmos. Chem. Phys.*, 10, 10003–10015, doi:10.5194/acp-10-10003-2010, 2010. 28963

Unterstrasser, S., Gierens, K., and Spichtinger, P.: The evolution of contrail microphysics in the vortex phase, *Meteorol. Z.*, 17, 145–156, 2008. 28941, 28948, 28950

Unterstrasser, S., Paoli, R., Söhlch, I., Kühnlein, C., and Gerz, T.: Dimension of aircraft exhaust plumes at cruise conditions: effect of wake vortices, *Atmos. Chem. Phys.*, 14, 2713–2733, doi:10.5194/acp-14-2713-2014, 2014. 28942, 28949, 28957, 28961

Voigt, C., Schumann, U., Jessberger, P., Jurkat, T., Petzold, A., Gayet, J.-F., Krämer, M., Thornberry, T., and Fahey, D.: Extinction and optical depth of contrails, *Geophys. Res. Lett.*, 38, L11806, doi:10.1029/2011GL047189, 2011. 28966

Yu, F. and Turco, R. P.: Contrail formation and impacts on aerosol properties in aircraft plumes: Effects of fuel sulfur content, *Geophys. Res. Lett.*, 25, 313–316, 1998. 28963

5

10

Properties of young contrails – a parametrisation based on large eddy simulations

S. Unterstrasser

Table 1. List of aircraft-dependent parameters. Columns 2–7: values used in UG2014; Cols. 8–10: values used in Naiman et al. (2011); Col. 11: values used in Paugam et al. (2010); Col. 12: values used in Picot et al. (2015).

aircraft type	CRJ	A320 B737	A300 B767	A350 B777	B747	A380	B737N	B767N	B747N	B747P1	B747P2
wing span b/m	21.2	34.4	47.6	60.9	64.4	79.8	34.3	47.2	64.5	59.9	59.9
circulation $\Gamma_0/(m^2 s^{-1})$	130	240	390	520	590	720	246	391	646	600	565
water vapour emission $\mathcal{V}/(gm^{-1})$	1.77	3.70	7.26	15.0	13.8	20.0	3.13	7.25	14.5	12.5	15.0
descent speed $w_0/(m s^{-1})$	1.24	1.41	1.66	1.73	1.85	1.83	1.45	1.68	2.03	2.03	1.91
vortex time scale t_0/s	13.4	19.1	22.5	27.6	27.3	34.3	18.5	22.0	24.9	23.1	24.6

Table A1. List of symbols.

symbol	value/unit	meaning
b	m	wing span
b_0	m	vortex separation
e_v, e_s	Pa	partial/saturation pressure of water vapour
f_N	1	normalised ice crystal number
f_{Ns}	1	fraction of surviving ice crystals
$\hat{f}_{Ns}, \tilde{f}_{Ns}$	1	parametrisations of f_{Ns}
\dot{m}_f	kg s^{-1}	fuel flow rate
$\hat{n}_{\text{mean}}, n_{\text{mean}}$	m^{-1}	(parametrised) ice crystal number concentration
r_p	m	radius of (intermediate) plume/contrail
r_{SD}	1	width of lognormal size distribution
s	s^{-1}	vertical wind shear
s_i	1	ambient supersaturation
x_s	1	coefficient of the parametrisation, > 0
Z_{atm}	m	supersaturation length scale
Z_{desc}	m	vertical displacement of vortex system, vortex length scale
\hat{Z}_{desc}	m	analytical approximation of Z_{desc}
Z_{emit}	m	emission length scale
Z_Δ	m	balance length scale
A	m^2	contrail area
A_p	m^2	cross-sectional area of (intermediate) plume/contrail
EI_{iceno}	$(\text{kg fuel})^{-1}$	ice crystal “emission” index
EI_{iceno}^*	1	normalised ice crystal “emission” index, $= EI_{\text{iceno}} / EI_{\text{iceno, ref}}$
$EI_{\text{iceno, ref}}$	$(\text{kg fuel})^{-1}$	reference ice crystal “emission” index, $2.8 \times 10^{14} \text{ kg}^{-1}$

Table A1. Continued.

symbol	value/unit	meaning
EI_{H_2O}	$\text{kg} (\text{kg fuel})^{-1}$	water vapour emission index, = 1.25
H, \hat{H}	m	simulated and parametrised contrail depth
I_v	kg m^{-2}	vertical profile of ice crystal mass
N_v	m^{-2}	vertical profile of ice crystal number
N_{BV}	s^{-1}	Brunt–Väisälä frequency
N	m^{-1}	Ice crystal number per flight metre
N_{form}	m^{-1}	Number of generated ice crystals per flight metre
N_{soot}	m^{-1}	Number of emitted soot particles per flight metre
N_{surv}	m^{-1}	Number of ice crystals per flight metre per flight metre after vortex break-up
R_{init}	m	radius of initial discs with ice crystals
R_v	$461 \text{ J kg}^{-1} \text{ K}^{-1}$	gas constant of water vapour
RH_i	1	ambient relative humidity with respect to ice
T_{CA}	K	temperature at cruise altitude
U	m s^{-1}	cruise speed of aircraft
\hat{W}, W	m	(parametrised) contrail width
W_{rect}	m	width of area-equivalent rectangle
$\alpha_{\text{atm}}, \alpha_{\text{emit}}$	1	coefficients of the parametrisation, > 0
$\alpha_{\text{desc}}, \alpha_0$	1	coefficients of the parametrisation, > 0
β_0, β_1	1	coefficients of the parametrisation, > 0
η_1, η_2	1	coefficients of the parametrisation, > 0
$\gamma_{\text{atm}}, \gamma_{\text{emit}}$	1	coefficients of the parametrisation, > 0
ρ_{air}	kg m^{-3}	density of air
ρ_{emit}	kg m^{-3}	emitted “concentration”
Γ_0	$\text{m}^2 \text{ s}^{-1}$	initial circulation of vortex
Γ_d	9.8 K km^{-1}	dry adiabatic lapse rate
ν	kg m^{-1}	water vapour emission

Properties of young contrails – a parametrisation based on large eddy simulations

S. Unterstrasser

[Title Page](#)

[Abstract](#)

[Introduction](#)

[Conclusions](#)

[References](#)

[Tables](#)

[Figures](#)

[|◀](#)

[▶|](#)

[◀](#)

[▶](#)

[Back](#)

[Close](#)

[Full Screen / Esc](#)

[Printer-friendly Version](#)

[Interactive Discussion](#)

Table A2. List of simulations. Columns 2–7 list parameter settings, Cols. 8–11 the simulated and approximated values for survival fraction and contrail depth, Cols. 12–14 the values of three characteristic length scales. “–1” indicates missing values. The aircraft (AC) type defines the wake vortex properties and water vapor emission as listed in Table 1.

#	T_{CA} K	RH _i %	N_{BV} s^{-1}	AC	EI_{cen0} m^{-1}	ν $g m^{-1}$	f_{Ns}	\hat{f}_{Ns}	H m	\hat{H} m	z_{atm} m	z_{emit} m	\hat{z}_{desc} m
Block 1 basic variation of RH _i and T_{CA} for B777, taken from U2014, Fig. 4													
0	209	100	1.15	B777	2.80×10^{14}	15.00	31.2	38.4	330	416	0	279	339
1	209	120	1.15	B777	2.80×10^{14}	15.00	89.9	88.2	420	441	137	279	339
2	212	100	1.15	B777	2.80×10^{14}	15.00	15.8	14.2	250	289	0	202	339
3	212	120	1.15	B777	2.80×10^{14}	15.00	81.8	80.5	420	437	141	202	339
4	212	140	1.15	B777	2.80×10^{14}	15.00	96.5	93.8	440	444	263	202	339
5	217	100	1.15	B777	2.80×10^{14}	15.00	3.3	2.8	110	57	0	117	339
6	217	110	1.15	B777	2.80×10^{14}	15.00	28.1	21.5	345	407	77	117	339
7	217	120	1.15	B777	2.80×10^{14}	15.00	65.6	62.5	420	428	148	117	339
8	217	130	1.15	B777	2.80×10^{14}	15.00	84.6	83.6	440	439	214	117	339
9	217	140	1.15	B777	2.80×10^{14}	15.00	92.8	90.9	450	443	276	117	339
10	222	100	1.15	B777	2.80×10^{14}	15.00	0.3	0.0	40	0	0	68	339
11	222	110	1.15	B777	2.80×10^{14}	15.00	16.4	11.6	180	235	81	68	339
12	222	120	1.15	B777	2.80×10^{14}	15.00	51.8	47.0	430	420	155	68	339
13	222	140	1.15	B777	2.80×10^{14}	15.00	89.4	89.1	460	442	289	68	339
14	225	110	1.15	B777	2.80×10^{14}	15.00	10.8	9.1	200	184	83	50	339
15	225	120	1.15	B777	2.80×10^{14}	15.00	44.5	41.7	450	418	160	50	339
16	225	130	1.15	B777	2.80×10^{14}	15.00	73.0	76.9	440	436	231	50	339
Block 2 basic RH _i -variation for various aircraft types, taken from UG2014, Fig. 2													
17	217	100	1.15	CRJ	2.80×10^{14}	1.77	4.7	9.9	135	100	0	90	169
18	217	100	1.15	B737	2.80×10^{14}	3.70	3.1	4.9	80	68	0	83	230
19	217	100	1.15	B767	2.80×10^{14}	7.26	2.0	2.6	80	45	0	91	293
20	217	100	1.15	B747	2.80×10^{14}	13.82	4.3	0.5	120	11	0	98	361
21	217	100	1.15	A380	2.80×10^{14}	20.03	1.6	0.0	160	0	0	96	399
22	217	120	1.15	CRJ	2.80×10^{14}	1.77	95.6	78.2	220	218	148	90	169
23	217	120	1.15	B737	2.80×10^{14}	3.70	89.9	69.5	315	293	148	83	230
24	217	120	1.15	B767	2.80×10^{14}	7.26	76.2	61.4	340	370	148	91	293
25	217	120	1.15	B747	2.80×10^{14}	13.82	56.4	50.6	440	450	148	98	361
26	217	120	1.15	A380	2.80×10^{14}	20.03	51.4	40.8	460	491	148	96	399
27	217	140	1.15	CRJ	2.80×10^{14}	1.77	99.9	93.6	220	222	276	90	169
28	217	140	1.15	B737	2.80×10^{14}	3.70	99.4	92.0	320	301	276	83	230
29	217	140	1.15	B767	2.80×10^{14}	7.26	96.5	90.8	370	383	276	91	293
30	217	140	1.15	B747	2.80×10^{14}	13.82	92.2	89.1	470	471	276	98	361
31	217	140	1.15	A380	2.80×10^{14}	20.03	89.9	87.4	490	519	276	96	399

Table A2. Continued.

#	T_{CA} K	RH _i %	N_{BV} s^{-1}	AC	EI_{lcoeno} m^{-1}	ν $g m^{-1}$	f_{Ns}	\hat{f}_{Ns}	H m	\hat{H} m	z_{atm} m	z_{emit} m	\hat{z}_{desc} m
Block 3													weaker thermal stratification, taken from UG2014, Fig. 5
32	217	140	0.50	CRJ	2.80×10^{14}	1.77	99.8	91.7	300	336	276	90	257
33	217	140	0.50	B737	2.80×10^{14}	3.70	92.8	88.4	380	455	276	83	349
34	217	140	0.50	B767	2.80×10^{14}	7.26	87.0	84.5	520	577	276	91	445
35	217	140	0.50	B777	2.80×10^{14}	15.00	66.5	83.5	650	666	276	117	514
36	217	140	0.50	B747	2.80×10^{14}	13.82	68.8	78.1	650	705	276	98	548
37	217	140	0.50	A380	2.80×10^{14}	20.03	62.3	70.9	670	772	276	96	605
38	217	120	0.50	CRJ	2.80×10^{14}	1.77	86.7	67.5	260	327	148	90	257
39	217	120	0.50	B737	2.80×10^{14}	3.70	63.8	46.5	400	433	148	83	349
40	217	120	0.50	B767	2.80×10^{14}	7.26	56.1	29.1	520	540	148	91	445
41	217	120	0.50	B777	2.80×10^{14}	15.00	31.9	25.8	620	622	148	117	514
42	217	120	0.50	B747	2.80×10^{14}	13.82	37.0	15.8	550	518	148	98	548
43	217	120	0.50	A380	2.80×10^{14}	20.03	29.8	9.6	550	350	148	96	605
Block 4													large variation of EI_{lcoeno} , for B777, taken from U2014, Fig. 9 right + additional new simulations
44	217	110	1.15	B777	1.40×10^{13}	15.00	54.1	78.2	400	407	77	117	339
45	217	120	1.15	B777	1.40×10^{13}	15.00	94.8	93.3	420	428	148	117	339
46	217	130	1.15	B777	1.40×10^{13}	15.00	99.8	97.3	440	439	214	117	339
47	217	110	1.15	B777	3.22×10^{13}	15.00	45.6	64.3	380	407	77	117	339
48	217	120	1.15	B777	3.22×10^{13}	15.00	90.3	89.3	420	428	148	117	339
49	217	130	1.15	B777	3.22×10^{13}	15.00	98.9	95.3	440	439	214	117	339
50	217	110	1.15	B777	5.40×10^{13}	15.00	40.9	52.8	370	407	77	117	339
51	217	120	1.15	B777	5.40×10^{13}	15.00	86.0	85.6	420	428	148	117	339
52	217	130	1.15	B777	5.40×10^{13}	15.00	97.6	93.5	440	439	214	117	339
53	217	110	1.15	B777	1.27×10^{14}	15.00	34.1	33.8	360	407	77	117	339
54	217	120	1.15	B777	1.27×10^{14}	15.00	76.5	76.4	420	428	148	117	339
55	217	130	1.15	B777	1.27×10^{14}	15.00	93.3	89.5	440	439	214	117	339
56	217	110	1.15	B777	6.09×10^{14}	15.00	20.7	14.1	345	407	77	117	339
57	217	120	1.15	B777	6.09×10^{14}	15.00	51.2	44.7	420	428	148	117	339
58	217	130	1.15	B777	6.09×10^{14}	15.00	70.1	74.1	440	439	214	117	339
59	217	110	1.15	B777	1.40×10^{15}	15.00	14.1	9.2	345	407	77	117	339
60	217	120	1.15	B777	1.40×10^{15}	15.00	35.5	28.1	420	428	148	117	339
61	217	130	1.15	B777	1.40×10^{15}	15.00	50.1	58.1	440	439	214	117	339
62	217	110	1.15	B777	3.22×10^{15}	15.00	9.0	6.0	345	407	77	117	339
63	217	120	1.15	B777	3.22×10^{15}	15.00	22.4	17.6	420	428	148	117	339
64	217	130	1.15	B777	3.22×10^{15}	15.00	31.7	38.9	440	439	214	117	339
65	217	110	1.15	B777	7.00×10^{15}	15.00	5.5	3.9	345	407	77	117	339
66	217	120	1.15	B777	7.00×10^{15}	15.00	19.5	11.6	420	428	148	117	339
67	217	130	1.15	B777	7.00×10^{15}	15.00	19.5	25.0	440	439	214	117	339

Properties of young contrails – a parametrisation based on large eddy simulations

S. Unterstrasser

#	T_{CA}	RH _i	N_{BV}	AC	Ei_{lenco}	ν	f_{Ns}	\hat{f}_{Ns}	H	\hat{H}	z_{atm}	z_{emit}	\hat{z}_{desc}
	K	%	s^{-1}		m^{-1}	$g m^{-1}$			m	m	m	m	m
Block 5 variation of fuel flow for B777, taken from U2014, Fig. 9 middle													
68	217	110	1.15	B777	2.80×10^{14}	12.00	22.8	15.8	320	322	77	95	339
69	217	110	1.15	B777	2.80×10^{14}	18.00	31.6	28.6	370	411	77	139	339
70	217	120	1.15	B777	2.80×10^{14}	12.00	64.7	54.0	420	424	148	95	339
71	217	120	1.15	B777	2.80×10^{14}	18.00	67.0	69.4	420	432	148	139	339
Block 6 small variation of Ei_{lenco} for all AC, taken from UG2014, Fig. 6													
72	217	120	1.15	CRJ	6.44×10^{13}	1.77	100.0	88.9	220	218	148	90	169
73	217	120	1.15	B737	6.44×10^{13}	3.70	98.5	85.4	315	293	148	83	230
74	217	120	1.15	B767	6.44×10^{13}	7.26	92.4	82.8	340	370	148	91	293
75	217	120	1.15	B747	6.44×10^{13}	13.82	75.6	79.1	440	450	148	98	361
76	217	120	1.15	A380	6.44×10^{13}	20.03	70.0	74.6	460	491	148	96	399
77	217	120	1.15	CRJ	1.22×10^{15}	1.77	70.1	58.4	220	218	148	90	169
78	217	120	1.15	B737	1.22×10^{15}	3.70	59.9	42.9	315	293	148	83	230
79	217	120	1.15	B767	1.22×10^{15}	7.26	47.4	31.6	340	370	148	91	293
80	217	120	1.15	B747	1.22×10^{15}	13.82	32.7	21.8	440	450	148	98	361
81	217	120	1.15	A380	1.22×10^{15}	20.03	29.5	16.1	460	491	148	96	399
f_{Ns} -values from Lewellen et al. (2014, Figs. 2, 9 and 10), H -values from Huebsch and Lewellen (2006, Fig. 6)													
82	205	110	0.88	B767	1.00×10^{15}	7.26	77.0	67.4	-1	435	69	339	335
83	205	130	0.88	B767	1.00×10^{15}	7.26	95.0	89.1	-1	440	191	339	335
84	218	110	0.86	B767	1.00×10^{15}	7.26	24.9	6.8	200	266	78	81	339
85	218	130	0.86	B767	1.00×10^{15}	7.26	48.0	55.6	470	437	216	81	339
86	225	110	0.84	B767	1.00×10^{15}	7.26	12.0	3.5	-1	147	83	38	343
87	225	130	0.84	B767	1.00×10^{15}	7.26	35.0	47.3	-1	440	231	38	343
88	218	110	0.86	B767	1.00×10^{17}	7.26	0.5	0.0	-1	266	78	81	339
89	218	110	0.86	B767	1.00×10^{16}	7.26	4.6	1.7	-1	266	78	81	339
90	218	110	0.86	B767	1.00×10^{14}	7.26	49.3	22.9	-1	266	78	81	339
91	218	110	0.86	B767	1.00×10^{13}	7.26	72.9	69.2	-1	266	78	81	339
92	218	110	0.86	B767	1.00×10^{12}	7.26	95.6	91.8	-1	266	78	81	339
93	218	110	0.86	B767	1.00×10^{11}	7.26	100.0	98.4	-1	266	78	81	339

28982

Properties of young contrails – a parametrisation based on large eddy simulations

S. Unterstrasser

[Title Page](#)

[Abstract](#)

[Introduction](#)

[Conclusions](#)

[References](#)

[Tables](#)

[Figures](#)

[|◀](#)

[▶|](#)

[◀](#)

[▶](#)

[Back](#)

[Close](#)

[Full Screen / Esc](#)

[Printer-friendly Version](#)

[Interactive Discussion](#)

Table A2. Continued.

#	T_{CA} K	RH _i %	N_{BY} s^{-1}	AC	EI_{iceno} m^{-1}	ν $g m^{-1}$	f_{Ns}	\hat{f}_{Ns}	H m	\hat{H} m	z_{atm} m	z_{emit} m	\hat{z}_{desc} m
f_{Ns} - and H -values from Naiman et al. (2011, Figs. 10, 11, 13 and 14)													
94	219	130	1.00	B767N	1.00×10^{15}	7.25	25.0	59.2	400	407	218	74	315
95	219	130	1.00	B747N	1.00×10^{15}	14.50	18.0	42.5	520	518	218	83	405
96	219	130	1.00	B737N	1.00×10^{15}	3.13	35.0	66.3	320	323	218	57	250
97	219	120	1.00	B767N	1.00×10^{15}	7.25	23.0	26.9	-1	393	151	74	315
98	219	110	1.00	B767N	1.00×10^{15}	7.25	21.0	7.8	-1	271	78	74	315
99	219	130	1.00	B767N	1.00×10^{14}	7.25	91.0	88.7	-1	407	218	74	315
100	219	110	1.00	B767N	1.00×10^{14}	7.25	88.0	24.5	-1	271	78	74	315
101	219	130	1.50	B767N	1.00×10^{15}	7.25	25.0	69.1	300	333	218	74	257
H -value from Paugam et al. (2010, Fig. 9)													
102	220	130	1.40	B747P1	1.50×10^{14}	12.50	-1.0	85.5	430	425	220	73	330
f_{Ns} - and H -values from Picot et al. (2015, Table 3, Fig. 13 and Fig. 19; pick simulations with Kelvin effect, if available)													
103	218	130	1.20	B747P2	8.30×10^{13}	15.00	98.0	91.2	440	447	216	108	346
104	218	110	1.20	B747P2	8.30×10^{13}	15.00	65.0	37.1	380	382	78	108	346
105	215	130	1.20	B747P2	8.30×10^{13}	15.00	99.0	93.0	-1	449	210	150	346

Properties of young contrails – a parametrisation based on large eddy simulations

S. Unterstrasser

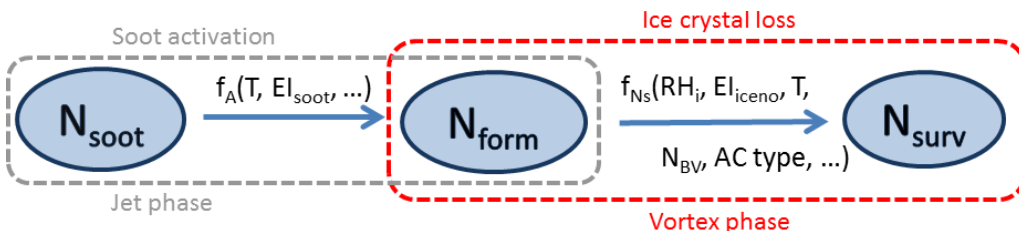


Figure 1. From soot emission to contrail ice crystal number: number of emitted soot particles N_{soot} , generated ice crystals N_{form} and ice crystals N_{surv} present after vortex breakup and relevant for contrail-to-cirrus transition. f_A denotes the fraction of activated soot particles (during the first seconds behind the aircraft), and f_{Ns} the fraction of ice crystals surviving the adiabatic heating during the vortex phase (during the first ~ 5 min). The displayed quantities have units “per metre (of flight path)” which can be converted into emission indices following Eq. (2) and analogous expressions. The present study focuses on the loss process during the vortex phase (red box). For soot-poor regimes (i.e. much lower than present-day EI_{soot} -values), contrail ice crystals originate mainly from ultrafine liquid and entrained ambient particles and the simple picture expressed by $N_{\text{form}} = f_A \times N_{\text{soot}}$ in the grey box is not valid any longer (Kärcher and Yu, 2009).

[Title Page](#)

[Abstract](#)

[Introduction](#)

[Conclusions](#)

[References](#)

[Tables](#)

[Figures](#)

◀

▶

◀

▶

[Back](#)

[Close](#)

[Full Screen / Esc](#)

[Printer-friendly Version](#)

[Interactive Discussion](#)

Properties of young contrails – a parametrisation based on large eddy simulations

S. Unterstrasser

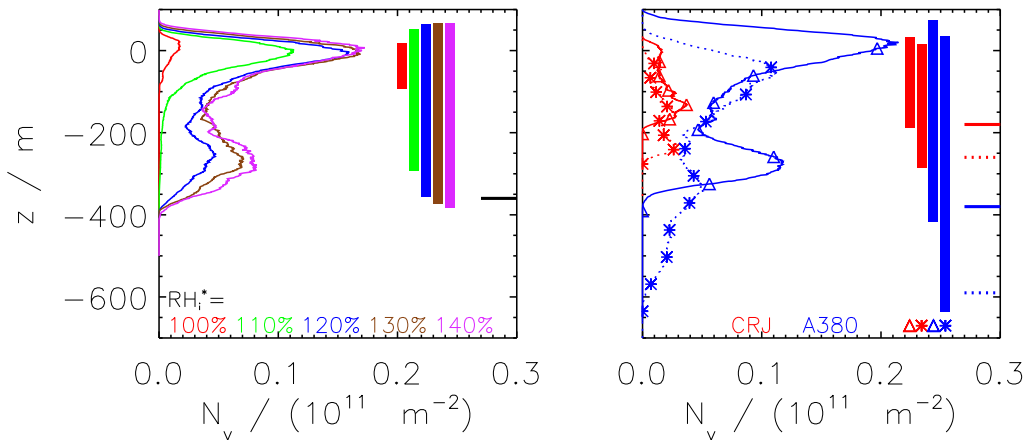


Figure 2. Vertical profiles of contrail ice crystal number after $t = 5\text{--}6\text{ min}$ (well after vortex break-up) are shown. The horizontal bars indicate the value of z_{desc} . The rectangles illustrate the vertical extent of the contrail and their heights are equal to the corresponding contrail depths H . Left panel: variation of relative humidity (see legend) for a B777-type aircraft and $N_{\text{BV}} = 0.0115\text{ s}^{-1}$. Right panel: variation of aircraft type (see legend) and stability (solid with triangles: $N_{\text{BV}} = 0.0115\text{ s}^{-1}$, dotted with stars: $N_{\text{BV}} = 0.005\text{ s}^{-1}$) for $\text{RH}_i = 140\%$. In all cases $T = 217\text{ K}$. The cruise altitude of the contrail generating aircraft is at $z = 0$.

Title Page

Abstract

Introduction

Conclusion

References

Tables

Figures

1

Back

Close

Full Screen / Esc

Interactive Discussion

**Properties of young contrails –
a parametrisation
based on large eddy
simulations**

S. Unterstrasser

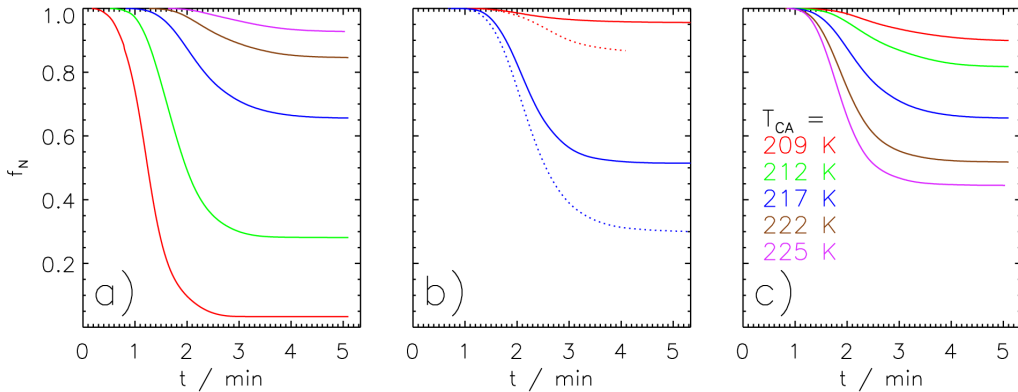


Figure 3. Temporal evolution of normalised ice crystal number is shown. Panels **(a)** and **(b)** as in Fig. 2, except that panel **(b)** shows simulations with $\text{RH}_i = 120\%$ instead of $\text{RH}_i = 140\%$. Panel **(c)** shows the effect of a temperature variation (see legend) at $\text{RH}_i = 120\%$ and $N_{\text{BV}} = 0.0115 \text{ s}^{-1}$.

Properties of young contrails – a parametrisation based on large eddy simulations

S. Unterstrasser

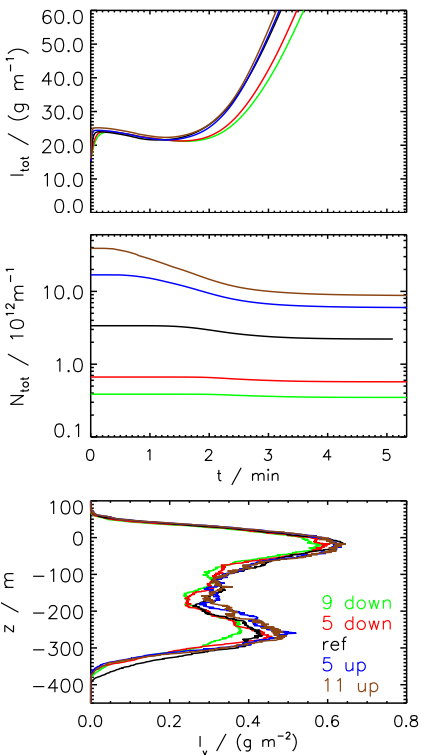


Figure 4. Variation of EI_{iceno} for a B777/A350-type aircraft, $\text{RH}_i = 120\%$, $T = 217\text{K}$ and $N_{\text{BV}} = 0.0115\text{s}^{-1}$. The reference simulation (“ref”) uses $\text{EI}_{\text{iceno, ref}} = 2.8 \times 10^{14}\text{kg}^{-1}$. In further simulations EI_{iceno} is lower or higher (see legend). Temporal evolution of total ice crystal mass (top) and number (middle) and vertical profiles of ice crystal mass after 5 min (bottom).

Properties of young contrails – a parametrisation based on large eddy simulations

S. Unterstrasser

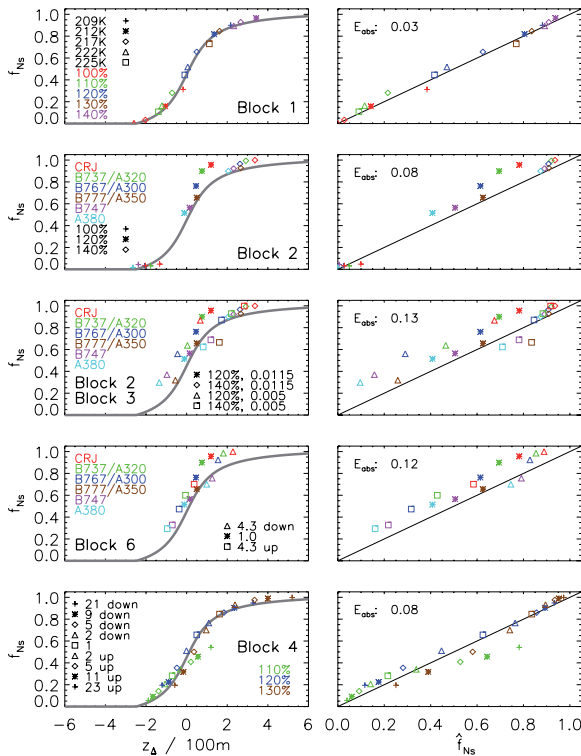


Figure 5. Left: Relationship between simulated survival fraction f_{Ns} and z_Δ . The grey curve shows the fit function \hat{a} as defined in Eq. (9). Right: Relationship between simulated survival fraction f_{Ns} and approximated survival fraction \hat{f}_{Ns} . The black line shows the 1–1 line. Each row shows a subset of simulations taken from various simulation blocks defined in Table A2. For example, the first row shows simulations of block 1, where RH_i and T_{CA} are varied. The legend in the plot provides a lists of the symbols and colours, which uniquely define the simulations parameters of each plotted data point.

Properties of young contrails – a parametrisation based on large eddy simulations

S. Unterstrasser

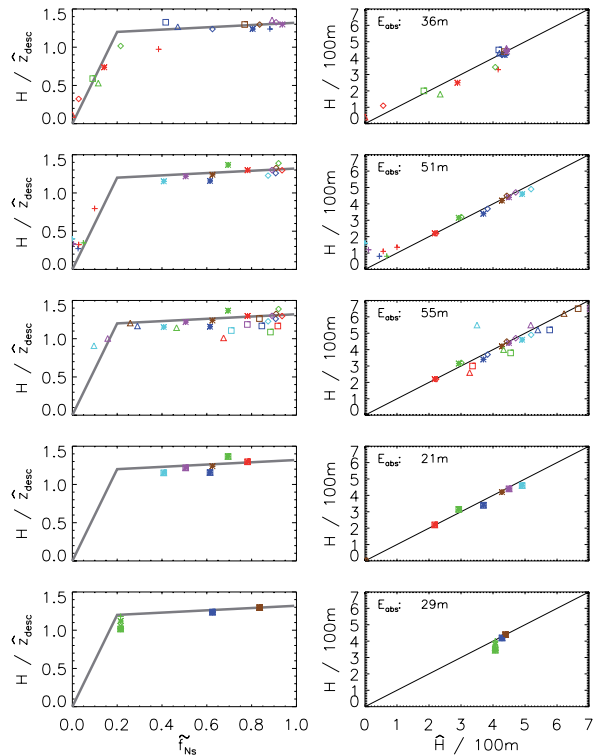


Figure 6. Left: Relationship between simulated contrail depth H over approximated \hat{z}_{desc} and approximated survival fraction \tilde{f}_{Ns} . The grey curve shows the fit function \hat{b} as defined in Eq. (13). Right: Relationship between simulated contrail depth H and approximated contrail depth \hat{H} . The simulation subsets and the layout are analogous to Fig. 5.

Properties of young contrails – a parametrisation based on large eddy simulations

S. Unterstrasser

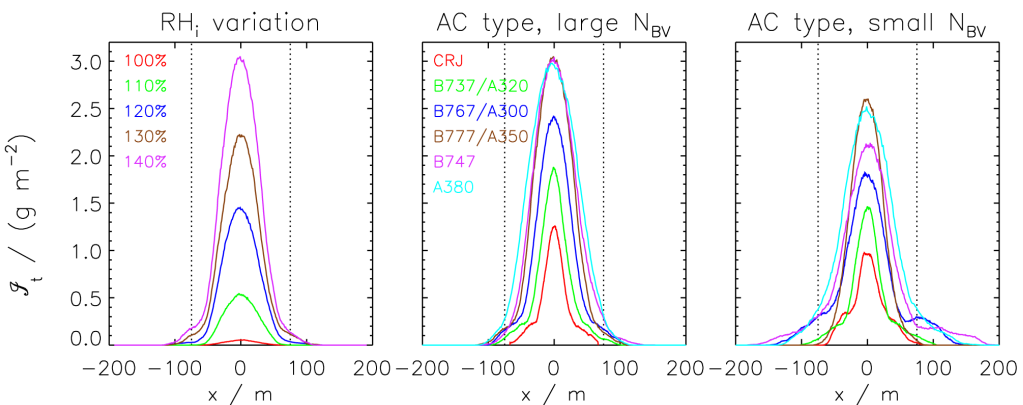


Figure 7. Transverse profiles of ice crystal mass for various simulation subsets. The profiles show ice water content integrated over the vertical direction and averaged along flight direction after 4 min. The left panel shows a RH_i -variation for a B777-type aircraft; the middle/right panel shows a variation of aircraft type for strong/weak stratification ($N_{\text{BV}} = 1.15 \times 10^{-2}$ and $0.5 \times 10^{-2} \text{ s}^{-1}$) at $\text{RH}_i = 120\%$. The simulations are listed in Block 1, 2 and 3 of Table A2, respectively. The dotted vertical lines indicate the $W = 150\text{ m}$ -approximation.

Title Page	
Abstract	Introduction
Conclusions	References
Tables	Figures
◀	▶
◀	▶
Back	Close
Full Screen / Esc	

[Printer-friendly Version](#)

Interactive Discussion

Properties of young contrails – a parametrisation based on large eddy simulations

S. Unterstrasser

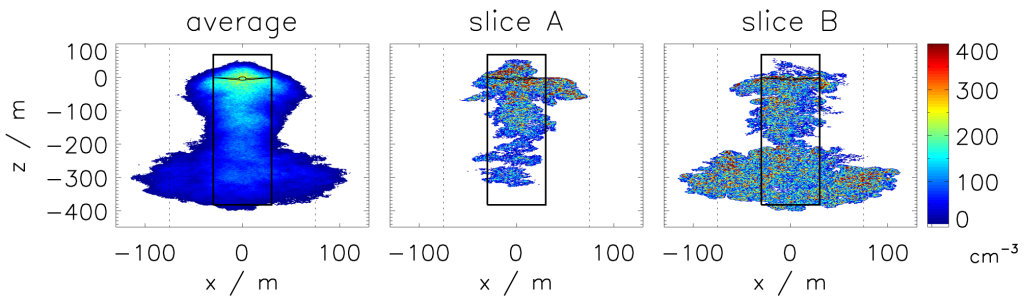


Figure 8. Ice crystal number concentrations in a plane normal to the flight direction after 4 min. The displayed simulation is # 9 from Table A2. In the left panel the number concentrations are summed up along flight direction and divided by the length of the flight segment. In the middle and right panel, two slices along flight direction are extracted. The dotted vertical lines indicate the $W = 150$ m-approximation (i.e. $x = \pm 75$ m). The black box indicates effective volume of the contrail. The box height equals the H value given in Table A2. The width W_{rect} is given by A/H , where A is the longitudinally averaged cross-section.

Properties of young contrails – a parametrisation based on large eddy simulations

S. Unterstrasser

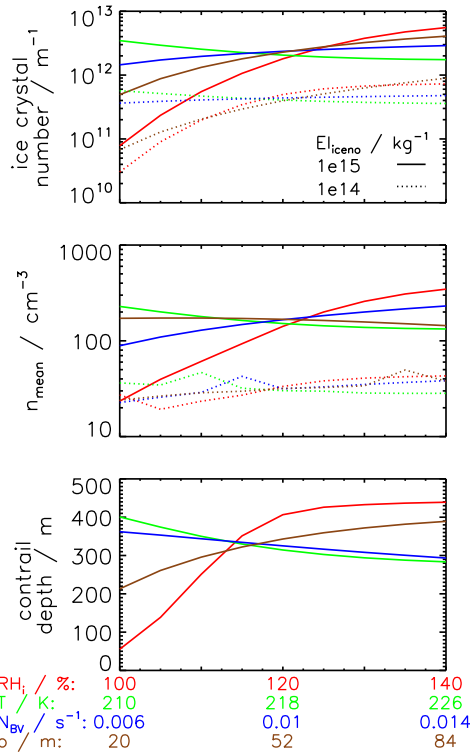


Figure 9. Ice crystal number per metre of flight path (top), mean ice crystal number concentration (middle) and contrail depth (bottom) after the vortex phase as a function of RH_i , T , N_{BV} or b . El_{iceno} is 10^{15} or 10^{14} kg^{-1} . The contrail depth parametrisation does not depend on El_{iceno} .

Properties of young contrails – a parametrisation based on large eddy simulations

S. Unterstrasser

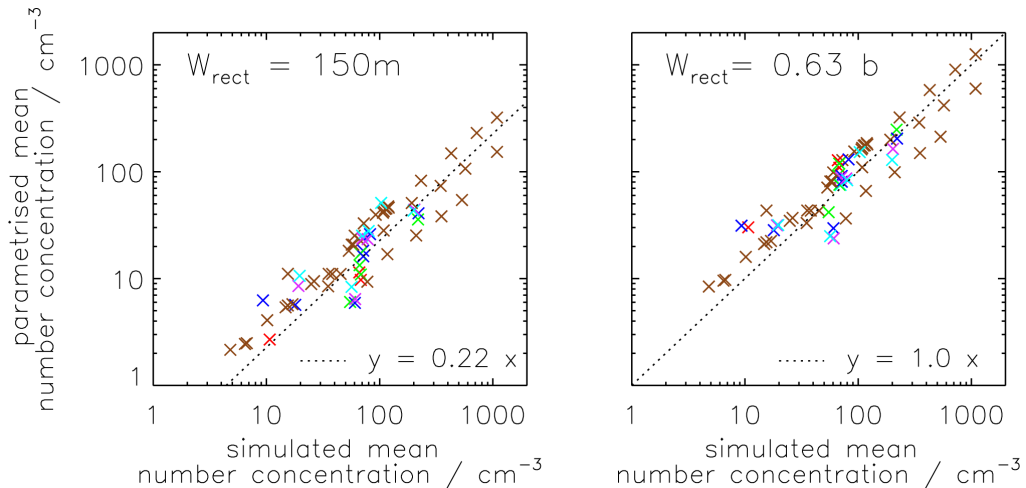


Figure 10. Simulated vs. parametrised mean ice crystal number concentration. In the simulation, the mean is taken over all grid boxes with non-zero ice crystal number concentration. The parametrised n_{mean} is given by $\hat{N}_{\text{surv}}/(\hat{H} W_{\text{rect}})$. In the left panel, W_{rect} is $\hat{W} = 150\text{m}$. In the right panel, \hat{W} is $0.63 b$, where b is the wing span.

Properties of young contrails – a parametrisation based on large eddy simulations

S. Unterstrasser

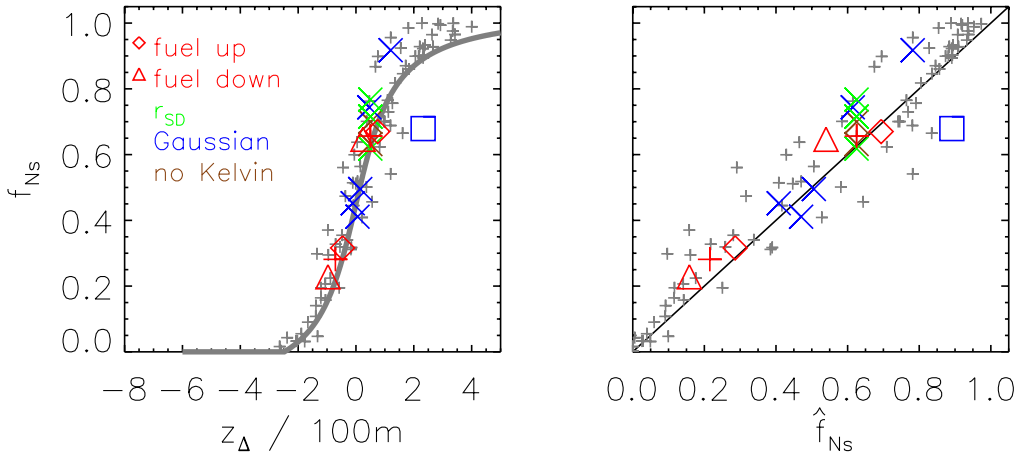


Figure 11. Plots as in Fig. 5. Grey symbols show all simulation data from Fig. 5. The coloured symbols show sensitivity simulations (see legend) not yet discussed.

- [Title Page](#)
- [Abstract](#) [Introduction](#)
- [Conclusions](#) [References](#)
- [Tables](#) [Figures](#)
- [◀](#) [▶](#)
- [◀](#) [▶](#)
- [Back](#) [Close](#)
- [Full Screen / Esc](#)
- [Printer-friendly Version](#)
- [Interactive Discussion](#)

Properties of young contrails – a parametrisation based on large eddy simulations

S. Unterstrasser

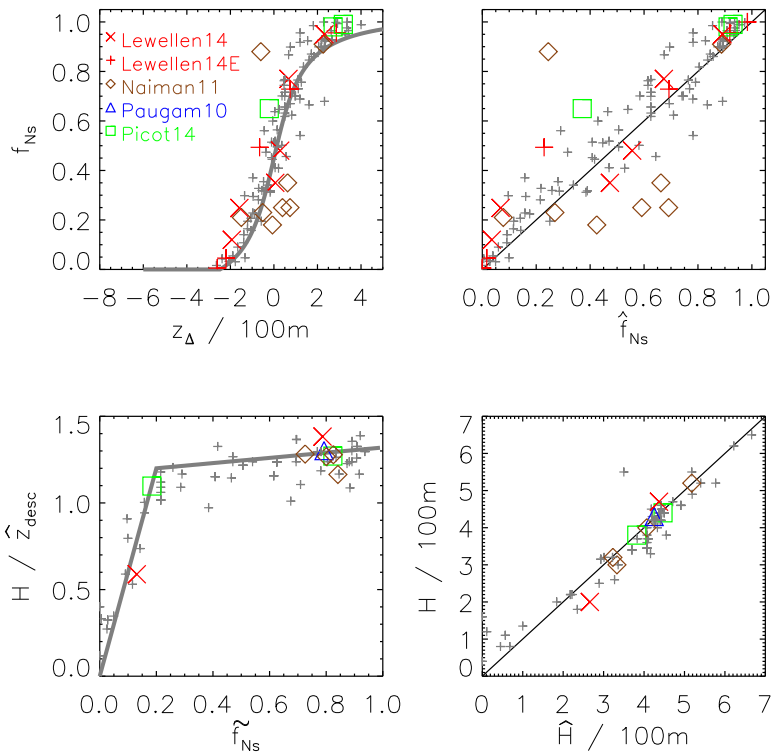


Figure 12. Top row: plot as in Fig. 5. Bottom row: plot as in Fig. 6. Grey symbols show all simulation data from Figs. 5 and 6. The coloured symbols show simulation results from other LES codes. Data are taken from Lewellen et al. (2014), Naiman et al. (2011), Paugam et al. (2010) and Picot et al. (2015).

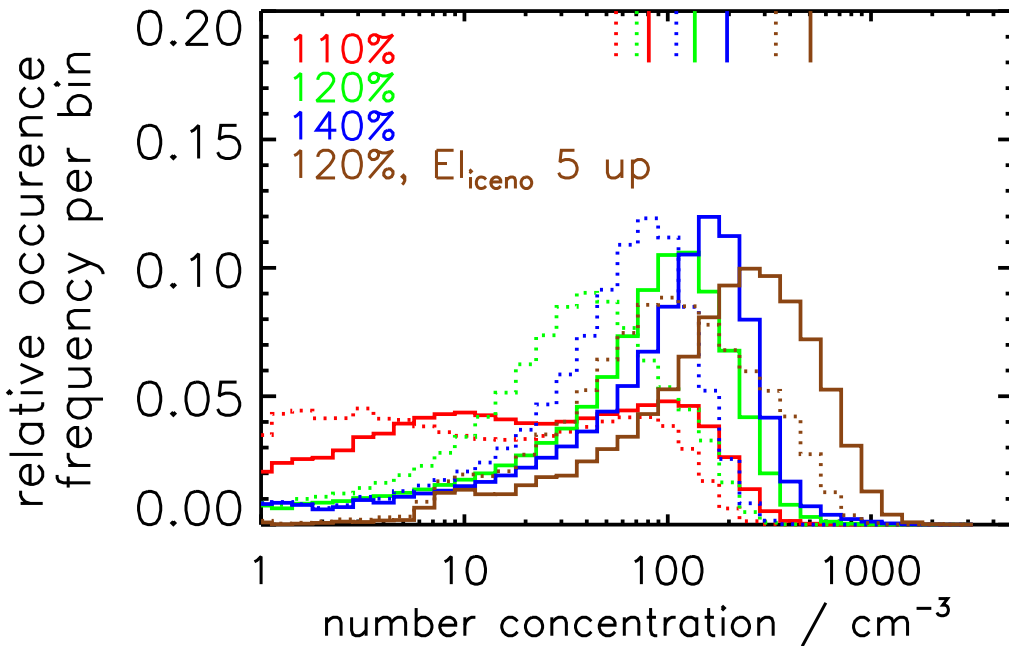


Figure 13. Relative occurrence frequencies of ice crystal number concentrations for various RH_i and an elevated EI_{iceno} (see legend). The according mean values are indicated by the vertical bars. Contrail age is 3 min (solid) or 5 min (dotted). The bin sizes increase exponentially.

Properties of young contrails – a parametrisation based on large eddy simulations

S. Unterstrasser

[Title Page](#)

[Abstract](#)

[Introduction](#)

[Conclusions](#)

[References](#)

[Tables](#)

[Figures](#)

[◀](#)

[▶](#)

[◀](#)

[▶](#)

[Back](#)

[Close](#)

[Full Screen / Esc](#)

[Printer-friendly Version](#)

[Interactive Discussion](#)

Properties of young contrails – a parametrisation based on large eddy simulations

S. Unterstrasser

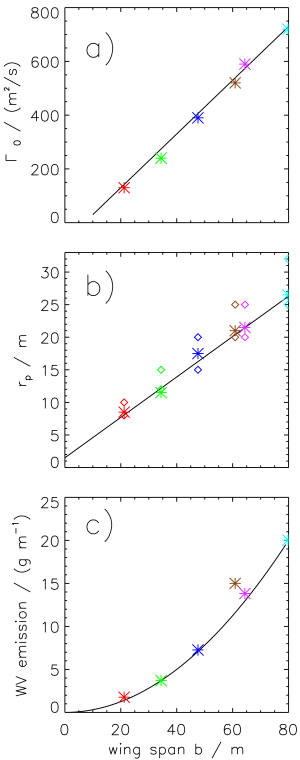


Figure A1. Top: Relationship between the initial wake vortex circulation Γ_0 and wing span b for medium aircraft mass as assumed in UG2014. The straight line shows the simple approximation $\Gamma_0 = (-70\text{ m} + 10\text{ }b)\text{ ms}^{-1}$. Middle: Relationship between the (intermediate) plume radius r_p and b . The straight line shows the simple approximation $1.5\text{ m} + 0.32\text{ }b$. The diamonds show two sets of initial plume radii as used in UG2014 Bottom: Relationship between water vapour emission \mathcal{V}_0 and b for medium fuel flow at cruise conditions as assumed in UG2014. The parabola shows the simple approximation $20\text{ g m}^{-1} \left(\frac{b}{80\text{ m}}\right)^2$.